The Planetary Science Journal, 7:98 (21pp), 2026 May https://doi.org/10.3847/PSJ/ae5c96

Mechanisms of Superrotation in Slowly Rotating and Tidally Locked Planets

Quentin Nicolas[1] and Geoffrey K. Vallis[2]

[1] Institute for Atmospheric and Climate Science, ETH Zurich, Zurich, Switzerland; quentin.nicolas@env.ethz.ch

[2] Department of Mathematics and Statistics, University of Exeter, Exeter, UK

Received 2025 October 7; revised 2026 March 17; accepted 2026 April 2; published 2026 May 5

Abstract

Superrotation is a common feature of quickly rotating gas giants (e.g., Jupiter), slowly rotating planetary bodies (e.g., Titan), and tidally locked planets. In this paper we compare and contrast the mechanisms of superrotation in slow rotators and tidally locked planets. We cover a wide range of planetary properties, in particular varying the thermal Rossby number Ro_T (controlled by planetary size, rotation rate, and instellation) and a radiative relaxation timescale T_{rad} (which parameterizes atmospheric optical thickness). We use a two-level primitive equation model that contains the principal mechanisms for superrotation in both regimes yet remains analytically tractable. Linearizations of the model elucidate the behavior of superrotation-inducing eddies. In tidally locked planets a baroclinic Matsuno–Gill-like structure arises in response to the zonal heating asymmetry but only produces superrotation when low-level drag is present. Nonlinear integrations further explore the superrotating regimes and exhibit significant time variability even in statistical equilibrium. Not all tidally locked regimes superrotate: subrotation arises at high T_{rad} (optically thick atmospheres) and weak low-level drag. On axisymmetrically forced slow rotators, superrotation is ubiquitously linked to a previously identified Rossby–Kelvin instability. The instability itself is also linked to the spin-up of superrotation in some tidally locked regimes. Finally, we explore the continuous transition in the mechanisms of superrotation from axisymmetrically forced to tidally locked planets by applying a progressively stronger zonally asymmetric equatorial forcing. The Matsuno–Gill pattern quickly dominates over traveling planetary Rossby–Kelvin waves in forcing superrotation, although both mechanisms can coexist. These results provide a unified view of superrotation mechanisms across a wide range of planetary bodies.

Unified Astronomy Thesaurus concepts: Exoplanet atmospheres (487); Atmospheric circulation (112); Exoplanet atmospheric dynamics (2307)

1. Introduction

Axisymmetric motion in planetary atmospheres cannot produce an angular momentum maximum away from a surface or an interior quiescent layer, a consequence of Hide's result (R. Hide 1969; G. K. Vallis 2017). Hence, equatorial winds must be zero or retrograde when the flow is purely axisymmetric. Despite this constraint, Venus, Jupiter, Saturn, Titan,[3] and many planetary atmospheres beyond the solar system have prograde equatorial winds; they *superrotate*. On these planets, nonaxisymmetric wave processes presumably transport momentum from extratropical and subtropical regions toward the equator.

At least three broad classes of planets exhibit superrotation: fast-rotating gas giants (e.g., Jupiter and Saturn), slowly rotating terrestrial bodies (e.g., Venus and Titan), and some tidally locked planets. Most observed exoplanets are tidally locked, if only because current detection techniques favor planets orbiting close to their host star, and tidal stresses are expected to rapidly bring such planets to a state of tidal locking (R. Barnes 2017). This last group contains both terrestrial planets and gas giants (the latter often referred to as hot Jupiters) and possibly other classes of planets.

Terrestrial planets are commonly "shallow," meaning that the depth of the layer in which atmospheric flows take place is small compared to the planet's radius. For such atmospheres, the primitive equations and shallow-water equations are very useful tools. Shallow flow can also occur in gas giants if the flows are confined to an upper stratified layer. On cold giants, such as Jupiter and Saturn, the flows seem to originate in, or at least extend into, a deeper convective layer (Y. Kaspi et al. 2020), and there the flow aligns with the rotation axis and shallow atmospheric models are inappropriate. On hot Jupiters, however, the internal heat flow is likely to be very weak compared to the stellar irradiation. The upper atmosphere may then be stably stratified and the flow shallow, as, for example, assumed by A. P. Showman et al. (2008). One might crudely estimate this depth as a density scale height, which is typically a factor of 20 or more smaller than the planetary radius. If these assumptions are applicable (even if not exact), both slowly rotating terrestrial planets and tidally locked hot Jupiters can be modeled in a single framework, that describing shallow atmospheres—or at least that is the approach we shall take here. (We, of course, do not discount the possibility that hot Jupiters have interesting internal dynamics.)

Given this, the question arises as to whether tidally locked and slowly rotating but axisymmetrically forced planets (henceforth referred to just as "slow rotators") share a common mechanism producing superrotation, or whether the mechanisms are fundamentally different. Various classes of waves have been proposed to drive superrotation in both cases.

---

[3] Titan's atmosphere shares similar properties (thickness, size, heating rate) with the atmospheres of some terrestrial planets, and here we simply regard it as a planetary atmosphere.

For the slow rotators an instability of the zonally symmetric basic state is likely required to create eddies, and one such instability (the Rossby–Kelvin (RK) instability) arises when midlatitude Rossby waves phase-lock with equatorial Kelvin waves and produce momentum-converging wind patterns (S. Iga & Y. Matsuda 2005; P. Wang & J. L. Mitchell 2014). For tidally locked planets, the steady linear response to nonaxisymmetric heating, namely a Matsuno–Gill-like pattern, can itself spin-up superrotation if vertical momentum transport (associated with a vertical mass transport due to heating) from a lower quiescent layer is also taken into account (A. P. Showman & L. M. Polvani 2011; S.-M. Tsai et al. 2014).

While shallow-water models have been immensely valuable in the exploration of superrotation mechanisms, producing realistic superrotation with these models has proved challenging. The vertical momentum transport parameterization employed by A. P. Showman & L. M. Polvani (2011) requires some amount of retrograde flow at the equator for superrotation to exist. The parameterization thus prevents the emergence of pan-equatorial superrotating flows such as found by global circulation models (GCMs) of tidally locked planets (e.g., A. P. Showman et al. 2009; R. T. Pierrehumbert & M. Hammond 2019). For slow rotators, P. Zurita-Gotor & I. M. Held (2018) have shown that a 1.5-layer shallow-water model, even with vertical momentum transport, struggles to produce realistic superrotation despite representing the RK instability.

The present work exploits a modeling framework that contains the simplest physical processes needed to produce more realistic superrotation (i.e., characteristic of that observed or simulated by full GCMs) in slow rotators and tidally locked planets. We seek to answer the following questions: Is it likely that all tidally locked planets superrotate? More specifically, for what sets of parameters (size, rotation rate, insolation, surface drag, etc.) does superrotation occur? Are the mechanisms of superrotation on tidally locked planets and slow rotators related? Can both coexist, or does one naturally dominate, and if so, under what circumstances?

Section 2 presents the two-level model used to address these questions. Section 3 explores the theoretical underpinnings of superrotation-inducing eddies on tidally locked planets and slow rotators in that model. In Section 4 the fully nonlinear version of the model is integrated into a statistically steady state for a wide range of planetary parameters, for both tidally locked planets and slow rotators. We specifically seek to map and understand the dependence of superrotation and the speed of the equatorial jet on two key parameters: a thermal Rossby number, and the rate of thermal relaxation. Section 5 presents a continuum of simulations that transitions from tidally locked to axisymmetrically forced states. These are used to probe the interplay between the momentum-converging eddies characteristic of both states. Concluding remarks can be found in Section 6.

Accepting that some readers will be more interested in the phenomenological and observational consequences than in the mathematical development, we provide more descriptive discussions in Sections 3.4, 4.3, and 6.

2. Methods

Perhaps the simplest models of superrotation are “1.5-layer” shallow-water models in which the vertical momentum transport from a lower quiescent layer is parameterized (A. P. Showman & L. M. Polvani 2010). These models do not contain baroclinic instabilities, and they have difficulties in producing superrotation in slowly rotating planets (e.g., P. Zurita-Gotor & I. M. Held 2018). To overcome these limitations while staying within a tractable framework, we choose to use a two-level hydrostatic primitive equation model, specifically that used by I. M. Held & M. J. Suarez (1978), M. J. Suarez & D. G. Duffy (1992), and R. Saravanan (1993), albeit with different parameters and forcings. The vertical discretization is illustrated in Figure 1. The lowest pressure level of the model, p_0, is taken as the mean surface pressure on a terrestrial planet; on a gas giant it is the pressure level at which horizontal flows become negligible compared to weather-layer flows. The governing equations for momentum, potential temperature, hydrostasy, and continuity read as

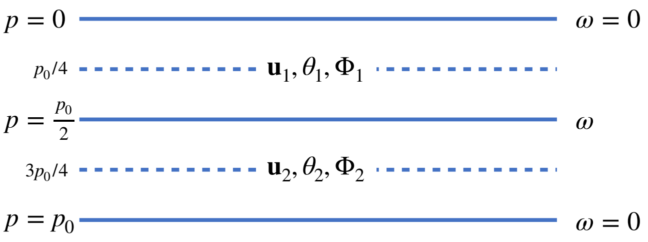

Figure 1. Vertical discretization of the two-level atmospheric model. A staggered grid is employed, where pressure velocity is defined on the full levels $p = 0$, $p_0/2$, and p_0 and horizontal velocities, geopotential heights, and potential temperatures are defined on the half levels $p_1 = p_0/4$ and $p_2 = 3p_0/4$.

$$\frac{\partial \boldsymbol{u}_i}{\partial t} + \boldsymbol{u}_i \cdot \nabla \boldsymbol{u}_i + \omega(\boldsymbol{u}_2 - \boldsymbol{u}_1) + f\boldsymbol{k} \times \boldsymbol{u}_i = -\nabla\Phi_i - \delta_{i2}\frac{\boldsymbol{u}_i}{\tau_{\mathrm{drag}}}, \quad i = 1, 2, \tag{1}$$

$$\frac{\partial \theta_i}{\partial t} + \boldsymbol{u}_i \cdot \nabla\theta_i + \omega(\theta_2 - \theta_1) = \frac{\theta_{iE} - \theta_i}{\tau_{\mathrm{rad}}}, \quad i = 1, 2, \tag{2}$$

$$\frac{\Phi_2 - \Phi_1}{\Pi_2 - \Pi_1} = -c_p\frac{\theta_1 + \theta_2}{2}, \tag{3}$$

$$\nabla \cdot \boldsymbol{u}_1 + 2\omega = 0, \tag{4}$$

$$\nabla \cdot \boldsymbol{u}_2 - 2\omega = 0, \tag{5}$$

where the subscript 1 describes the upper layer and the subscript 2 describes the lower layer. $\boldsymbol{u} = (u, v)$ is the horizontal velocity, ω the pressure velocity at the mid-level $p_0/2$ divided by p_0, Φ the geopotential height, and θ the potential temperature. $\Pi = (p/p_0)^{R/c_p}$ is the Exner function (G. K. Vallis 2017), where R is the specific gas constant and c_p the isobaric heat capacity (hereafter $R/c_p = 2/7$, as for a diatomic gas). Here $f = 2\Omega\sin\phi$ is the Coriolis parameter, where Ω is the planetary rotation rate and ϕ is latitude, and $\boldsymbol{k}$ is the vertical unit vector. A Rayleigh drag, with timescale τ_{drag}, is applied in the lower layer.

The thermodynamic forcing term consists of a relaxation toward a prescribed potential temperature profile $\theta_{iE}(\phi, \lambda)$, where λ denotes longitude, on a timescale τ_{rad}. We use

$$\theta_{iE}(\phi, \lambda) = \begin{cases} (\Delta\Theta_h - \Delta\Theta_v \ln\Pi_i)\cos\phi\,\max(0, \cos\lambda) & \text{for tidally locked planets}, \\ (\Delta\Theta_h - \Delta\Theta_v \ln\Pi_i)\cos\phi\,\dfrac{1}{\pi} & \text{for non-tidally locked planets}, \end{cases} \tag{6}$$

where $\Delta\Theta_h$ scales the equator-to-pole potential temperature contrast and $\Delta\Theta_v$ scales the vertical stratification of this reference profile. The meridional structure is taken to be proportional to that of the stellar irradiation in the absence of axial tilt (i.e., $\propto\cos\phi$). The same is true for the zonal structure on tidally locked planets: it varies as $\cos\lambda$ on the dayside and vanishes on the nightside. The factor $1/\pi$ in the second expression of Equation (6) ensures that the mean θ_E, a proxy for the stellar irradiation, is the same for tidally locked and non−tidally locked planets for given $\Delta\Theta_h$ and $\Delta\Theta_v$. Finally, the assumption of a zonally symmetric forcing for non−tidally locked planets is adequate when the thermal relaxation scale τ_{rad} is much longer than the planet's rotation period $2\pi/\Omega$ (K. Ohno & X. Zhang 2019). This is not the case, for example, on Venus: there the effect of thermal tides is of primary importance (e.g., M. Takagi & Y. Matsuda 2007). In this paper, we shall consider planets for which $2\Omega\tau_{\mathrm{rad}}$ is between 10 and 1000; the above constraint is marginally verified at the lower end of this range and well satisfied elsewhere.

To reduce the number of model parameters, we nondimensionalize Equations (1)–(5) following S. F. Potter et al. (2014). Scaling length with a (the planetary radius), time with $(2\Omega)^{-1}$, potential temperature with $\Delta\Theta_h$, geopotential with $c_p\Delta\Theta_h$, horizontal velocity with $c_p\Delta\Theta_h/(2\Omega a)$ (from geostrophic balance), and vertical velocity with $c_p\Delta\Theta_h/(2\Omega a^2)$, the governing equations become

$$\begin{aligned}\frac{\partial \boldsymbol{u}_i}{\partial t} &+ \mathrm{Ro}_T(\boldsymbol{u}_i\cdot\nabla\boldsymbol{u}_i + \omega(\boldsymbol{u}_2-\boldsymbol{u}_1)) + f\boldsymbol{k}\times\boldsymbol{u}_i\\ &= -\nabla\Phi_i - \delta_{i2}E\boldsymbol{u}_i,\quad i=1,2,\end{aligned}\tag{7}$$

$$\frac{\partial \theta_i}{\partial t} + \mathrm{Ro}_T(\boldsymbol{u}_i\cdot\nabla\theta_i + \omega(\theta_2-\theta_1)) = \frac{\theta_{iE}-\theta_i}{T_{\mathrm{rad}}},\quad i=1,2,\tag{8}$$

$$\Phi_2-\Phi_1 = -\gamma(\theta_1+\theta_2),\tag{9}$$

$$\nabla\cdot\boldsymbol{u}_1 + 2\omega = 0,\tag{10}$$

$$\nabla\cdot\boldsymbol{u}_2 - 2\omega = 0,\tag{11}$$

where all quantities are now nondimensional (including $f=\sin\phi$) and $\gamma=(\Pi_2-\Pi_1)/2\simeq 0.12$. Four nondimensional control parameters appear: a thermal Rossby number, an Ekman number, a nondimensional thermal relaxation timescale, and a stratification parameter (controlling the vertical structure of θ_E), given respectively by

$$\begin{aligned}\mathrm{Ro}_T &= \frac{c_p\Delta\Theta_h}{(2\Omega a)^2},\quad E=\frac{1}{2\Omega\tau_{\mathrm{drag}}},\\ T_{\mathrm{rad}} &= 2\Omega\tau_{\mathrm{rad}},\quad \mathcal{S}=\Delta\Theta_v/\Delta\Theta_h.\end{aligned}\tag{12}$$

Ro_T is a fundamental parameter for planetary atmospheres: like the classical Rossby number, it measures the importance of inertial acceleration with respect to the Coriolis effect, but it uses a velocity scale derived from thermal wind balance. For small Rossby numbers, we expect the flow to be strongly constrained by rotation, potentially with large temperature gradients and narrow jets. Larger Rossby numbers are associated with weaker temperature gradients and broader circulations: in the framework of this paper, where the forcing temperature vanishes at the poles, Ro_T is approximately the square of the "weak temperature gradient parameter" Λ of R. T. Pierrehumbert & M. Hammond (2019).

Numerical integrations on the sphere are performed using Dedalus (K. J. Burns et al. 2020). In addition to the fluid equations themselves, we use a small fourth-order horizontal hyperdiffusion in the momentum and thermodynamic equations to damp the enstrophy and tracer cascades at high wavenumbers, with values tuned to ensure numerical stability.

3. Quasi-linear Processes Driving Superrotation

We now investigate the nature of the eddies that can drive superrotation. We do this by linearizing the model about basic states representative of tidally locked planets and slow rotators and then examining the nature of the resulting eddy momentum fluxes. We begin by reviewing the formulae and properties of these eddy fluxes in the two-level model, and then we explore two classes of planetary-scale waves in tidally locked planets and slow rotators that provide a net eastward momentum flux at the equator, that is, that can accelerate superrotation. We summarize the important results in Section 3.4.

3.1. Eddy Momentum Fluxes in the Two-level Model

Denoting zonal averages with an overbar, the zonal-mean zonal momentum equation in the frictionless upper layer reads

$$\frac{\partial \overline{u_1}}{\partial t} = \overline{(f+\mathrm{Ro}_T\zeta_1)v_1} - \mathrm{Ro}_T\,\overline{\omega(u_2-u_1)},\tag{13}$$

where ζ_1 is the relative vorticity of the upper layer, and we have used the identity $\boldsymbol{u}_1\cdot\nabla\,\boldsymbol{u}_1 = (1/2)\,\nabla\,(\boldsymbol{u}_1\cdot\boldsymbol{u}_1) + \zeta_1\boldsymbol{k}\times\boldsymbol{u}_1$; the term in $\partial_\lambda(\boldsymbol{u}_1\cdot\boldsymbol{u}_1)$ vanishes upon zonal averaging. For a circulation that is equatorially symmetric at all times, $v_1=0$ at the equator, so that the only term that can accelerate the equatorial jet is the vertical momentum transport term in Equation (13). Hence, superrotation requires $\overline{\omega(u_2-u_1)}<0$ at the equator, meaning that vertical motion needs to generate a flux of eastward momentum from the lower to the upper layer. A related condition for superrotation exists in 1.5-layer shallow-water models, but the absence of lower-layer flow ($u_2=0$) implies that the equatorial jet must be westward at some longitudes (A. P. Showman & L. M. Polvani 2011); no such requirement exists in the two-level model. In continuously stratified cases, one similarly needs $\omega\partial_p u<0$ for superrotation with an equatorially symmetric circulation.

Decomposing each field into a zonal mean and a deviation from that mean (denoted with a prime), Equation (13) can be divided into contributions from the mean flow and eddy fields. The eddy momentum flux convergence (EMFC) is

$$\begin{aligned}\mathrm{EMFC}_1 &= \mathrm{Ro}_T(\overline{\zeta_1'v_1'} - \overline{\omega'(u_2-u_1)'})\\ &= -\mathrm{Ro}_T\left(\frac{1}{\cos^2\phi}\frac{\partial}{\partial\phi}(\overline{u_1'v_1'}\cos^2\phi) + \overline{\omega'(u_1+u_2)'}\right),\end{aligned}\tag{14}$$

where the second equality results from the expression of the vorticity in spherical coordinates and the continuity equation. A similar exercise in the lower layer yields

$$\begin{aligned}\mathrm{EMFC}_2 &= \mathrm{Ro}_T(\overline{\zeta_2'v_2'} - \overline{\omega'(u_2-u_1)'})\\ &= -\mathrm{Ro}_T\left(\frac{1}{\cos^2\phi}\frac{\partial}{\partial\phi}(\overline{u_2'v_2'}\cos^2\phi) - \overline{\omega'(u_1+u_2)'}\right).\end{aligned}\tag{15}$$

Equations (14) and (15) express the EMFC in both advective form and flux form, offering complementary views that lead to two important takeaways. First, the vertical convergence of eddy momentum fluxes redistributes zonal momentum from one layer to the other: $\omega'(u_1 + u_2)'$ appears with opposite signs in the flux form of the upper- and lower-layer EMFCs. Second, if the eddies are equatorially symmetric, the EMFC must be equal in both layers at the equator. Indeed, for such eddies $v_i' = 0$ at the equator and the advective form gives $\mathrm{EMFC}_1 = \mathrm{EMFC}_2 = -\mathrm{Ro}_T\overline{\omega'(u_2 - u_1)'}$. A further consequence is that superrotation cannot merely arise from eddies that diverge eastward momentum in the lower layer and converge it in the upper layer (i.e., simply acting through the $\omega'(u_1 + u_2)'$ term in the flux-form expression): nonzero horizontal convergence is required; otherwise, the flux-form expression gives $\mathrm{EMFC}_1 = -\mathrm{EMFC}_2$, which means that both must vanish. In particular, a mechanism such as the quasi-biennial oscillation on Earth (M. P. Baldwin et al. 2001), which produces intermittent superrotation in the stratosphere through vertical convergence of eddy momentum fluxes, cannot be captured. In a continuously stratified atmosphere, the equatorial EMFC of symmetric eddies reads $\overline{\omega'\partial u'/\partial p}$ and need not be vertically uniform: this constraint only applies in a two-level model.

3.2. Tidally Locked Planets

Tidally locked planets are driven by a zonally and meridionally varying thermal forcing. Because the cooling is nearly uniform on the nightside, while the heating is much stronger near the equator on the dayside, there is a gradient of zonal-mean heating between the equator and the poles. Formally, one can expand the nondimensional version of the equilibrium potential temperature profile (6) in a Fourier series in longitude:

$$\theta_{iE}(\phi, \lambda) = \left(\frac{1}{\pi} + \frac{1}{2}\cos\lambda + \frac{2}{3\pi}\cos 2\lambda + \dots\right) \times (1 - \mathcal{S}\ln\Pi_i)\cos\phi. \tag{16}$$

One may then regard the total circulation as a sum of the response to the first term (an axisymmetric thermal forcing) and the second term (a wavenumber 1 forcing), neglecting the $\cos 2\lambda$ term and higher-order terms in the expansion.

The axisymmetric part of the forcing does not of itself induce superrotation since it leads to a thermally direct axisymmetric circulation, which simply exports angular momentum away from the equator. Further, the eastward midlatitude jets arising from this circulation may be baroclinically unstable, generating Rossby waves that deposit westward momentum equatorward of their source region (G. K. Vallis 2017).

However, the response to the wavenumber 1 forcing will not be axisymmetric and can directly lead to superrotation. The linear response is a Matsuno–Gill-like circulation pattern,[4] as noted by A. P. Showman & L. M. Polvani (2010) in a shallow-water context. Here we extend the analysis to two layers, allowing the vertical transport to occur naturally. The required equations are obtained by linearizing Equations (1)–(5) about a state of rest with uniform potential temperatures Θ_1 and Θ_2 (perturbations from that basic state are denoted with primes). We assume $\Theta_1 - \Theta_2 = \mathcal{S}$; note that steady-state stratification in the nonlinear simulations of Section 4 is between $\mathcal{S}$ and $4\mathcal{S}$,

$$f\mathbf{k} \times \mathbf{u}_1' + \nabla\Phi_1' = 0, \tag{17a}$$

$$f\mathbf{k} \times \mathbf{u}_2' + \nabla\Phi_2' + E\mathbf{u}_2' = 0, \tag{17b}$$

$$-\mathcal{S}\mathrm{Ro}_T\omega' = \frac{\theta_{1E}' - \theta_1'}{T_{\mathrm{rad}}}, \tag{17c}$$

$$-\mathcal{S}\mathrm{Ro}_T\omega' = \frac{\theta_{2E}' - \theta_2'}{T_{\mathrm{rad}}}, \tag{17d}$$

along with continuity and hydrostasy. Here $\theta_{iE}' = \cos\phi\cos\lambda\,(1 - \mathcal{S}\ln\Pi_i)/2$ for $i = 1, 2$.

A sample solution of Equations (17a)–(17d), solved on the sphere with $E = 0.02$, $\mathcal{S} = 0.05$, and $\mathcal{S}\mathrm{Ro}_T T_{\mathrm{rad}} = 1$, is shown in Figure 2. The lower-layer geopotential field (Figure 2(c)) illustrates the classical structure of the response to equatorial heating, composed of an equatorial Kelvin wave and two off-equatorial Rossby waves that together form an eastward-pointing chevron pattern. The ensuing horizontal winds are such that $u_2'v_2' < 0$ north of the equator and $u_2'v_2' > 0$ south of the equator. This leads to horizontal convergence of momentum flux (Equation (15) and Figure 2(d), dashed line). The vertical convergence term cancels half of the horizontal convergence term at the equator (Figure 2(d), dotted line). In the upper layer, the absence of drag mandates that the eddy geopotential field be uniform at the equator (Figure 2(a)). There is no chevron-like pattern, and the horizontal winds do not converge eastward momentum at low latitudes (Figure 2(b), dashed line). However, we saw in Section 3.1 that for such an equatorially symmetric mode the total EMFC must be equal in both layers at the equator; there should thus be positive EMFC in the upper layer, as in the lower layer. This is achieved thanks to the vertical convergence term, which is equal and opposite to that in the lower layer (Figure 2(b), dotted line). The two-layer Matsuno–Gill pattern thus leads to eastward equatorial acceleration in *both* layers.

3.2.1. Dependence of EMFC on Planetary Parameters

To understand how the acceleration depends on the various control parameters, note that the solution to Equations (17a)–(17d) mainly depends on two parameters: the product $\mathcal{S}\mathrm{Ro}_T T_{\mathrm{rad}}$ and E (there is an additional weaker dependence on $\mathcal{S}$ through the magnitudes of θ_{1E} and θ_{2E}). Figure 3(a) shows sample solutions of the upper-layer EMFC where both of these parameters are varied. The product $\mathcal{S}\mathrm{Ro}_T T_{\mathrm{rad}}$ modulates both the strength and meridional pattern of the EMFC. An analytical solution for the flow and its EMFC is obtained in Appendix A in the drag-free ($E = 0$) case. We show that the EMFC has two off-equatorial maxima that scale as $\mathrm{Ro}_T^{-1}\mathcal{S}^{-2}T_{\mathrm{rad}}^{-2}$. Figure 3(a) (dashed lines) shows the meridional pattern of EMFC obtained analytically for $E = 0$ and two values of $\mathcal{S}\mathrm{Ro}_T T_{\mathrm{rad}}$, scaled by $\mathrm{Ro}_T\mathcal{S}^2 T_{\mathrm{rad}}^2$ so that they have comparable magnitudes. The off-equatorial maxima shift equatorward as $\mathcal{S}\mathrm{Ro}_T T_{\mathrm{rad}}$ is decreased. This happens because the nondimensional Rossby radius (Equation (A3)) scales as $(\mathcal{S}\mathrm{Ro}_T T_{\mathrm{rad}})^{1/4}$ in this problem; hence, the waves are more equatorially confined as $\mathcal{S}\mathrm{Ro}_T T_{\mathrm{rad}}$ is decreased. For small $E > 0$, the solutions, obtained numerically, retain the same qualitative features away from the equator (Figure 3(a), solid lines).

---

[4] T. Matsuno (1966) first studied the problem of the linear response of Earth's tropical atmosphere to a sinusoidal heat source with a particular meridional structure. A. E. Gill (1980) extended this work to isolated heat sources with arbitrary meridional structures. The problem studied here is closer to Matsuno's.

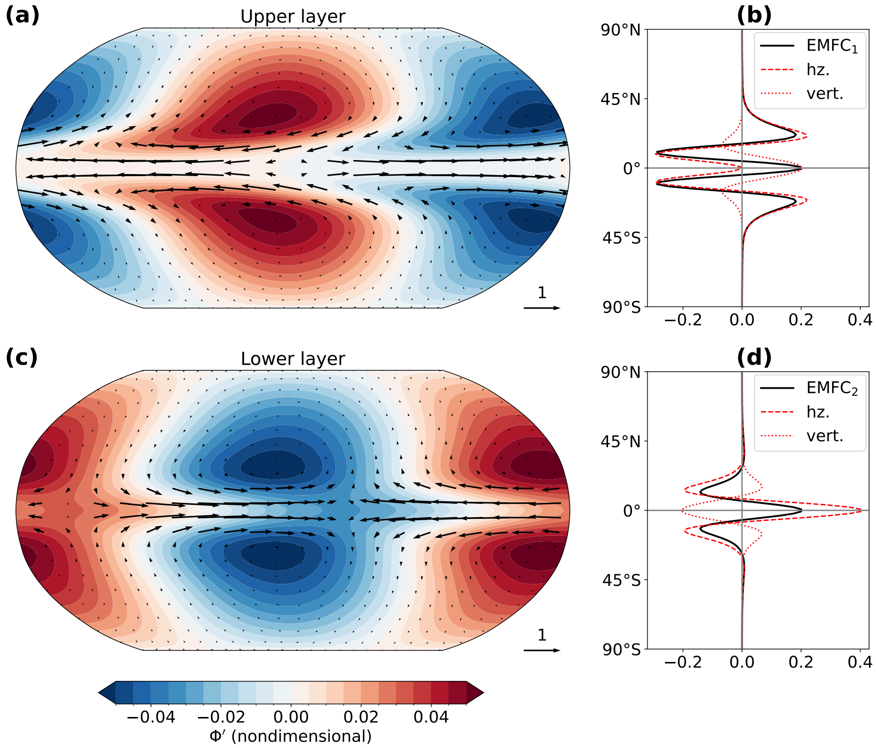

Figure 2. Numerical solution of the Matsuno–Gill problem (Equations (17a)–(17d)) with $E = 0.02$ and $\mathcal{S}\mathrm{Ro}_T T_{\mathrm{rad}} = 1$, and its EMFC. (a) Upper-layer geopotential Φ_1' (shading) and wind $\boldsymbol{u}_1'$ (arrows). (b) EMFC in the upper layer (solid), its horizontal convergence component (red dashed), and its vertical convergence component (red dotted line; see Equation (14), flux-form expression). (c, d) Same as panels (a) and (b), except for the lower layer.

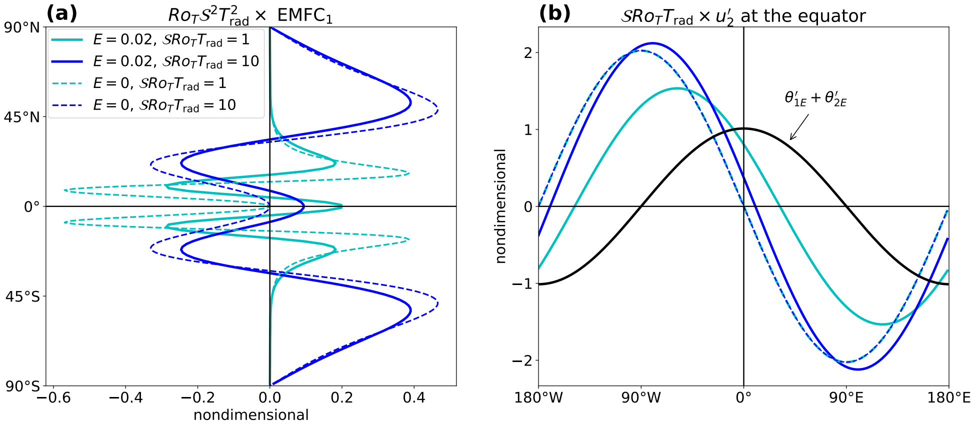

Figure 3. Gill model properties on the sphere with different input parameters. (a) Scaled upper-layer EMFC. (b) Scaled lower-layer zonal wind u_2' at the equator. Note the eastward shift in u_2' with increased E and $\mathcal{S}\mathrm{Ro}_T T_{\mathrm{rad}}$. The black line shows the vertically integrated reference potential temperature profile at the equator. Drag-free solutions (dashed) are obtained analytically in Appendix A. Solutions with low-level drag (solid) are obtained numerically.

The lower-layer drag E primarily affects the equatorial EMFC (compare solid and dashed lines in Figure 3(a)). It is positive for $E > 0$ but vanishes when $E = 0$. We provide two explanations for this behavior: the first one is rather qualitative but conceptually simpler, and the second one is quantitative but more involved. The qualitative explanation starts with the fact that in the absence of drag the geopotential field must be uniform at the equator (evaluate Equation (17b) with $E = 0$ at the equator). This prevents the existence of the chevron-like pattern leading to horizontal EMFC in the lower layer. Because horizontal EMFC is also zero in the upper layer and vertical EMFC can only redistribute fluxes vertically (see Section 3.1), the total EMFC is thus zero in both layers.

Analytically, the $E = 0$ behavior can be understood using the vorticity balance, which reads in the upper layer as

$$-2f\omega' + \beta v_1' = 0, \tag{18}$$

where $\beta = \partial_\phi f = \cos\phi$. At the equator, the meridional derivative of Equation (18) is $-2\beta\omega' + \beta\partial_\phi v_1' = 0$. Combining with continuity and dividing by β, one obtains $4\omega' = -\partial_\lambda u_1'$, implying that

$$\overline{\omega' u_1'} = 0 \text{ at the equator.} \tag{19}$$

When $E = 0$, one similarly shows that $\overline{\omega' u_2'} = 0$; thus, the EMFC (which is $-\mathrm{Ro}_T\,\overline{\omega'(u_2' - u_1')}$) at the equator for an equatorially symmetric circulation) is zero. What happens when $E > 0$? We show in Appendix B that the upper-layer equatorial EMFC is

$$\mathrm{EMFC}_1 = \frac{1}{\mathcal{S}T_{\mathrm{rad}}}\overline{(\theta'_{1E} + \theta'_{2E})u'_2} \text{ at the equator.} \tag{20}$$

In Figure 3(b), we show patterns of $u'_2(\lambda)$ at the equator for all the above solutions. When $E = 0$, $\theta'_{1E} + \theta'_{2E}$ (which acts as a proxy for vertical motion) and u'_2 are exactly in quadrature (they have a 90° phase shift), and $\overline{(\theta'_{1E} + \theta'_{2E})u'_2} = 0$. When friction is included, the low-level wind pattern shifts eastward (solid lines in Figure 3(b)), which allows for vertical motion to transfer eastward momentum to the upper layer. Interestingly, the shift is more pronounced as $\mathcal{S}\mathrm{Ro}_T T_{\mathrm{rad}}$ is decreased. This explains why the equatorial peak in EMFC strengthens relative to its off-equatorial counterparts as $\mathcal{S}\mathrm{Ro}_T T_{\mathrm{rad}}$ is decreased in Figure 3(a).

The eastward shift in the low-level zonal wind is hard to capture analytically in the two-level model, but it can be understood in the beta-plane shallow-water Matsuno–Gill problem. We show in Appendix C that the equatorial zonal wind field is the sum of Rossby wave and Kelvin wave components, which are both in quadrature with the heating field in the absence of drag. When the drag increases, the Rossby component shifts eastward while the Kelvin component shifts westward. The Rossby component's shift is more pronounced, and its zonal wind field is three times stronger; hence, the sum of both components shifts eastward. Decreased $\mathcal{S}\mathrm{Ro}_T T_{\mathrm{rad}}$ is akin to an increase in thermal damping in the two-level model (Equations (17c)–(17d)). This explains why the shift in u_2 is more pronounced at lower $\mathcal{S}\mathrm{Ro}_T T_{\mathrm{rad}}$ in Figure 3(b), and ultimately why the equatorial acceleration is then stronger (relative to the off-equatorial peaks) in Figure 3(a).

3.3. Slow Rotators

In our idealized picture, non−tidally locked planets have an entirely zonally symmetric forcing and a solution in the form of a non-superrotating, axisymmetric circulation exists. Thus, another mechanism is needed to produce nonaxisymmetric eddies that can accelerate the equatorial atmosphere, and indeed S. Iga & Y. Matsuda (2005) found that the interaction of midlatitude Rossby waves with an equatorial Kelvin wave (the "RK mode") can give rise to an instability producing eastward EMFC. Although the pattern of this instability resembles in some ways the Matsuno–Gill pattern, the mode does not arise as a response to a stationary forcing and has a nonzero eastward propagation speed. P. Wang & J. L. Mitchell (2014) extended the analysis using a primitive equation model and found that an unstable RK mode can exist whenever the midlatitude jets Doppler-shift the Rossby wave phase speed to match that of the equatorial Kelvin wave. A physical proximity of the Rossby and Kelvin waves is also needed; otherwise, the interaction is weak, and it is zero if there is no overlap at all.

Being symmetric about the equator, the RK mode cannot accelerate superrotation there in the absence of vertical momentum transport. Consequently, single-layer shallow-water models cannot produce superrotation by that mechanism if vertical momentum transport is not parameterized, and they struggle to do so even when it is (P. Zurita-Gotor & I. M. Held 2018). However, RK modes that produce equatorial acceleration can be naturally captured in the two-level model. To show this, we linearize Equations (1)–(5) about a state of horizontally uniform potential temperatures Θ_1 and Θ_2 (with $\Theta_1 - \Theta_2 = \mathcal{S}$), with a barotropic background zonal wind $\boldsymbol{U} = (U(\phi), 0)$ and without friction (the modes still appear in the presence of friction—we are merely trying to show that friction is not a necessary component here). The equations read as

$$\partial_t \boldsymbol{u}'_i + \mathrm{Ro}_T(\boldsymbol{U}\cdot\nabla\boldsymbol{u}'_i + \boldsymbol{u}'_i\cdot\nabla\boldsymbol{U}) + f\boldsymbol{k}\times\boldsymbol{u}'_i + \nabla\Phi'_i = 0, \quad i = 1, 2, \tag{21}$$

$$\partial_t \theta'_i + \mathrm{Ro}_T(\boldsymbol{U}\cdot\nabla\theta'_i - \mathcal{S}\omega') + \frac{\theta'_i}{T_{\mathrm{rad}}} = 0, \qquad i = 1, 2, \tag{22}$$

[along with continuity and hydrostasy. $\boldsymbol{u}'_i$, θ'_i and Φ'_i are perturbation quantities. Following P. Zurita-Gotor & I. M. Held (2018), $U(\phi)$ has two broad midlatitude jets centered on a latitude ϕ_0 (here taken as 50°). $U(\phi)$ is defined in terms of its vorticity ζ; a parameter α governs the strength of the jets, with strong, angular-momentum-conserving jets for $\alpha = 0$ and no wind for $\alpha = 1$:

$$\zeta(\phi) = \frac{1}{\mathrm{Ro}_T}\begin{cases}(\alpha - 1)f, & |\phi| < \phi_0\\ (\cos^{-2}\phi_0 - \alpha\tan^2\phi_0 - 1)f, & |\phi| > \phi_0\end{cases} \tag{23}$$

$$U(\phi) = -\frac{1}{\cos\phi}\int_0^{\phi}\zeta\cos\phi\, d\phi. \tag{24}$$

Equations (21)–(22) can be split into independent barotropic and baroclinic modes. Summing Equation (21) for both layers and summing Equations (10)–(11), the barotropic mode (denoted with a double overbar, i.e., $\bar{\bar{\boldsymbol{u}}} = \boldsymbol{u}'_1 + \boldsymbol{u}'_2$ and $\bar{\bar{\Phi}} = \Phi'_1 + \Phi'_2$) verifies

$$\partial_t\bar{\bar{\boldsymbol{u}}} + \mathrm{Ro}_T(\boldsymbol{U}\cdot\nabla\bar{\bar{\boldsymbol{u}}} + \bar{\bar{\boldsymbol{u}}}\cdot\nabla\boldsymbol{U}) + f\boldsymbol{k}\times\bar{\bar{\boldsymbol{u}}} + \nabla\bar{\bar{\Phi}} = 0, \tag{25}$$

$$\nabla\cdot\bar{\bar{\boldsymbol{u}}} = 0. \tag{26}$$

Subtracting Equation (21) between both layers and combining the sum of Equation (22) over both layers with Equations (9)–(11) yields the equations governing the baroclinic mode (denoted with a hat, i.e., $\hat{\boldsymbol{u}} = \boldsymbol{u}'_1 - \boldsymbol{u}'_2$ and $\hat{\Phi} = \Phi'_1 - \Phi'_2$):

$$\partial_t\hat{\boldsymbol{u}} + \mathrm{Ro}_T(\boldsymbol{U}\cdot\nabla\hat{\boldsymbol{u}} + \hat{\boldsymbol{u}}\cdot\nabla\boldsymbol{U}) + f\boldsymbol{k}\times\hat{\boldsymbol{u}} + \nabla\hat{\Phi} = 0, \tag{27}$$

$$\partial_t\hat{\Phi} + \mathrm{Ro}_T\boldsymbol{U}\cdot\nabla\hat{\Phi} + \frac{\gamma\mathcal{S}\mathrm{Ro}_T}{2}\nabla\cdot\hat{\boldsymbol{u}} + \frac{\hat{\Phi}}{T_{\mathrm{rad}}} = 0. \tag{28}$$

The baroclinic mode equations (Equations (27)–(28)) are exactly equivalent to a single-layer shallow-water system, with a gravity wave speed

$$c = \sqrt{\frac{\gamma\mathcal{S}}{2\mathrm{Ro}_T}} \tag{29}$$

(Ro_T appears in the denominator because of our convention for the nondimensionalization of velocities). The barotropic mode, being nondivergent, cannot support Kelvin waves, so we expect RK waves to be associated with the baroclinic part of the flow.

The ability of the Rossby and Kelvin waves to phase-lock depends on two conditions: they must have equal phase speeds, and they must physically overlap meridionally. The phase speed of midlatitude Rossby waves is on the order of

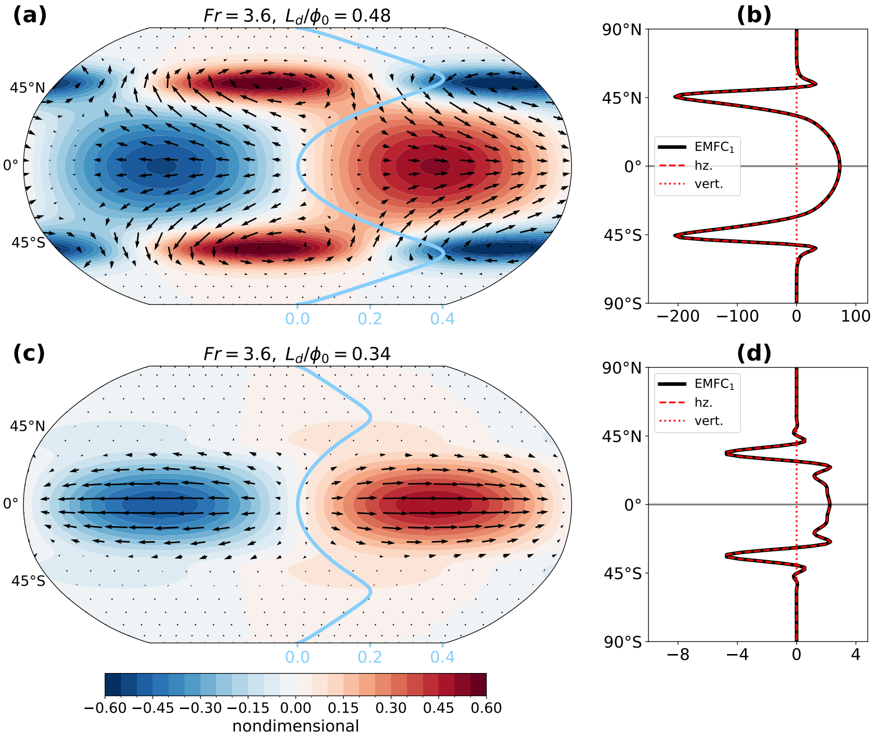

Figure 4. RK eigenmodes with $E = 0$, $\mathcal{S} = 0.05$, and $T_{\rm rad} = 200$. (a) Upper-layer geopotential Φ_1' (shading) and wind $\boldsymbol{u}_1'$ (arrows), for $\mathrm{Ro}_T = 10$ and $\alpha = 0$, corresponding to $\mathrm{Fr} = 3.6$ and $L_d/\phi_0 = 0.48$. The thick blue line shows the local Rossby number, i.e., Ro_T times the background wind profile (scale at the bottom of the panel). (b) Upper-layer EMFC and its decomposition, as in Figure 2(b). (c, d) Same as panels (a) and (b), except with $\mathrm{Ro}_T = 2.5$ and $\alpha = 0.5$, corresponding to $\mathrm{Fr} = 3.6$ and $L_d\phi_0 = 0.34$. The mode amplitudes are normalized by their mean upper-layer kinetic energy.

the background wind speed $U(\phi_0)$, while that of the Kelvin waves is c. The two waves have equal angular phase speeds if the Froude number $\mathrm{Fr} = [U(\phi_0)/\cos\phi_0]/c$ is of order unity (P. Wang & J. L. Mitchell 2014; the factor $1/\cos\phi_0$ transforms the Rossby wave's phase speed into an angular velocity). In practice, we will see that RK modes exist at values of Fr larger than 1, as the Kelvin wave is able to propagate faster than c. The second condition, that of spatial overlap, may be measured as the ratio of the meridional extent of Kelvin waves (given by the equatorial Rossby radius $L_d = \sqrt{\mathrm{Ro}_T c}$) to the Rossby wave latitude ϕ_0 measured in radians.

We solve for $k = 1$ eigenmodes of the system given by Equations (21)–(22) with two different sets of input parameters (hereafter k denotes the zonal wavenumber). Anticipating the simulation results of Section 4.2, where the spatial overlap condition will prove more restrictive than that on Fr, we chose to vary the former and fix the latter. We fix $T_{\rm rad} = 200$ and $\mathcal{S} = 0.05$ and choose $\mathrm{Ro}_T = 10$, $\alpha = 0$ (a small/slowly rotating planet with angular-momentum-conserving jets that has $\mathrm{Fr} = 3.6$ and $L_d/\phi_0 = 0.48$) and $\mathrm{Ro}_T = 2.5$, $\alpha = 0.5$ (a larger/faster-rotating planet with weaker jets that has $\mathrm{Fr} = 3.6$ and $L_d/\phi_0 = 0.34$) as test cases.

In the first case (Figure 4(a)), the most unstable mode has a typical RK pattern, with a broad equatorial Kelvin wave (due to the large deformation radius) coupling with Rossby waves propagating along the jets. The resulting eastward-pointing chevron pattern yields horizontal convergence of eastward momentum flux in a broad region from 30°S to 30°N (Figure 4(b), dashed red line). The mode is purely baroclinic ($\boldsymbol{u}_1' + \boldsymbol{u}_2' = 0$, not shown). As a result, the vertical convergence of momentum fluxes $-\mathrm{Ro}_T\overline{\omega'(u_1' + u_2')}$ vanishes (Figure 4(b), dotted red line). Thus, positive equatorial EMFC results from the horizontal convergence term only. This is opposite to the Matsuno–Gill pattern, for which the horizontal convergence term vanishes at the equator in the upper layer, while the vertical convergence term carries the positive EMFC (Figure 2(b)). In the RK mode of Figure 4(a), the chevron pattern in the geopotential exists despite the absence of drag, because equatorial geopotential gradients can be balanced by the $\partial_t u_i'$ term in Equation (21). This is unlike the Matsuno–Gill problem, which is steady and hence for which no term can balance equatorial geopotential gradients in the absence of drag. This is ultimately why the horizontal and vertical convergence terms behave differently in the two problems. The mode has an eigenfrequency of 0.23, close to the theoretical frequency of the $k = 1$ equatorial Kelvin wave, $\mathrm{Ro}_T c = \sqrt{\gamma\mathcal{S}\mathrm{Ro}_T/2} \simeq 0.17$. It has a large growth rate (0.09, about 1 over a rotation period).

An RK mode is also present in the second case (Figures 4(c)–(d)). The Rossby and Kelvin components do not interact as strongly, as the meridional scale of the Kelvin wave is smaller, resulting in a weak negative growth rate and nearly vanishing equatorial EMFC. Further investigation suggests that with the values of $T_{\rm rad}$, $\mathcal{S}$, and ϕ_0 used in Figure 4, RK modes disappear below $L_d/\phi_0 \simeq 0.3$.

The dependence of the RK modes on Fr is worth commenting on. Although one may expect that Fr needs to be exactly 1 for Kelvin and Rossby waves to phase-lock, P. Wang & J. L. Mitchell (2014) found unstable RK modes up to $\mathrm{Fr} = 4$. This requires Rossby waves that are slower than the peak jet speed $U(\phi_0)$ (e.g., due to their intrinsic westward phase speed), Kelvin waves that are faster than c, or both. P. Wang & J. L. Mitchell (2014) attributed their finding to slower Rossby waves. We found (not shown) that unstable RK modes may exist up to $\mathrm{Fr} = 10$ and that the phase speed of the waves is weaker than the peak jet speed but can be 2–3 times faster than c. This happens as the meridional flow (which is zero in a classical Kelvin wave but can be large for RK modes) strengthens convergence at the equator.

3.4. Discussion of Quasi-linear Results

Quasi-linear theory suggests that superrotation in both axisymmetrically forced planets and tidally locked planets can arise through the interaction of Rossby and Kelvin waves, although there are import differences in the two cases. In the tidally locked case the circulation producing the superrotation is directly forced: the response to the zonal wavenumber 1 component of the heating, when treated linearly, is similar to a Matsuno–Gill pattern, with an eastward-extending equatorial Kelvin lobe and westward-extending off-equatorial Rossby gyres. Where drag is present (e.g., the lower layer of the two-level model), the familiar chevron shape that results leads to an EMFC at the equator, and so potentially to superrotation, and this is transmitted to upper levels by vertical momentum fluxes.

In some contrast, superrotation-inducing eddies on slow rotators are not directly forced but typically result from an instability, specifically an RK instability, in which an equatorial Kelvin wave phase-locks with off-equatorial Rossby waves that are Doppler-shifted by eastward jets. The instability arises even in the presence of a purely axisymmetric forcing. It is favored when the angular velocities of the waves are similar (as measured by Fr) and the waves overlap spatially (i.e., when L_d/ϕ_0 is large enough). As with the tidally locked case, vertical eddy momentum fluxes are an essential component of the mechanism.

In both cases key parameters are those governing the bottom drag, the thermal damping (and so the optical thickness of the atmosphere), and the rotation rate. In the absence of drag, equatorial geopotential gradients must vanish in the Matsuno–Gill model and the chevron pattern disappears, leading to zero EMFC at the equator on tidally locked planets. This is not true on slow rotators because time-dependent flows, in particular RK modes, support equatorial geopotential gradients even without drag. In the tidally locked case, the rate of thermal damping modulates the phase difference between the thermal forcing and the response to it; weaker thermal damping (higher T_{rad}) reduces this phase difference and leads to weaker equatorial EMFC. The influence of thermal damping on RK modes is not explored here, but it likely affects their growth rates. Finally, slower rotation (i.e., higher Ro_T) tends to meridionally broaden any pattern, because the equatorial deformation radius increases. In the axisymmetric case this enables there to be an interaction between the Kelvin and Rossby modes. In the tidally locked case, however, slower rotation is also akin to a decrease in thermal damping, which, as seen above, reduces the EMFC at the equator.

These factors may lead to differences between the responses of tidally locked gas giants and terrestrial planets, although quantifying that requires further study with more comprehensive models. In the next section we explore the effects of these various processes as nonlinearity becomes important.

4. Nonlinear Integrations over a Wide Range of Parameters

We now present results from fully nonlinear integrations of the model, with both tidally locked and axisymmetric thermal forcings, for a wide range of input parameters. Our goal is to test the qualitative, quasi-linear mechanisms presented in Section 3, including the behavior of superrotation as a function of Ro_T and T_{rad} and the importance of surface friction for superrotation on tidally locked planets.

4.1. Tidally Locked Planets

All of the runs initially presented in this section use $E = 0.02$ and $\mathcal{S} = 0.05$. These are both relatively low values—the value of E comes from an average of the drag coefficient over the lower half of the atmosphere in the model of I. M. Held & M. J. Suarez (1994), and the low value of $\mathcal{S}$ represents relaxation toward a profile that is nearly neutral to convection (but with a small positive value for numerical stability). We present runs with increased and zero friction at the end of this section. The presence of condensible species and/or stellar radiation absorbing species would likely increase the value of S, but we do not explore that here.[5] We perform a total of 121 runs, spanning two orders of magnitude in both Ro_T (with values 0.1, 0.15, 0.25, 0.4, 0.65, 1.0, 1.5, 2.5, 4.0, 6.5, 10.0) and T_{rad} (with values 10, 15, 25, 40, 65, 100, 150, 250, 400, 650, 1000). Each run is integrated for 1000 rotation periods, i.e., until $t = 4000\pi$. A statistically steady state is reached after about 300 rotation periods, and steady-state values are obtained by averaging over the last 700.

4.1.1. Equatorial Jet Strength and General Features

Figure 5(a) displays a regime diagram of the equilibrium equatorial jet speed in (Ro_T, T_{rad}) space. For $\mathrm{Ro}_T < 1$, the qualitative predictions from quasi-linear theory (Section 3.2) are verified: the jet speed decreases with both Ro_T and T_{rad}. For $\mathrm{Ro}_T \geqslant 1$, these predictions break down: while the jet speed mostly decreases with T_{rad}, it increases with Ro_T. It is not surprising that the Matsuno–Gill model loses quantitative accuracy when $\mathrm{Ro}_T \geqslant 1$, as Ro_T measures the importance of the nonlinear acceleration terms that it neglects. The behavior of the high-Ro_T regime is analyzed in further detail in Section 4.1.3. Another important point is that, at least in this two-level framework, not all tidally locked planets superrotate: with high enough T_{rad}, subrotation appears for all the values of Ro_T considered here. The transition between superrotation and subrotation does not happen abruptly in this (Ro_T, T_{rad}) phase space: several simulations lying at the boundary between these states spend their time oscillating between the two (see hatched area in Figure 5).

With the geostrophic scaling used in Figure 5(a), nondimensional wind speeds weaken with increasing Ro_T. Another way to nondimensionalize wind speeds would be to scale them by the planet's surface speed at the equator, Ωa (a factor of $2\mathrm{Ro}_T$ separates the former nondimensionalization from the latter). This scaling quantifies the excess angular momentum of the atmosphere relative to the planet's equatorial surface. Figure 5(b) shows that superrotating jets at high Ro_T generally exceed the planetary angular momentum by a larger fraction than at low Ro_T.

---

[5] Section 3 and S. F. Potter et al. (2014) suggest that variations in $\mathcal{S}$ may in some respects mimic variations in Ro_T, perhaps through their influence on the Rossby deformation radius. See also G. P. Williams (2006) and R. T. Pierrehumbert & M. Hammond (2019).

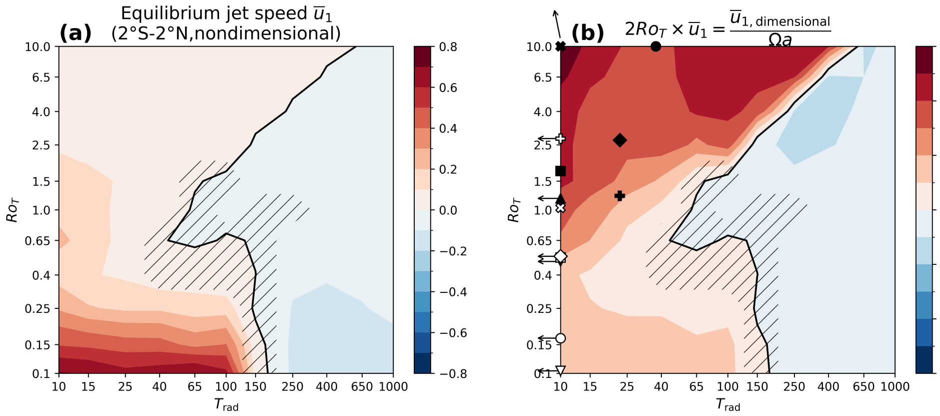

Figure 5. Equilibrium equatorial jet speed in tidally locked planets. (a) Upper-level zonal-mean zonal wind speed $\overline{u_1}$ averaged 2°S–2°N, as a function of Ro_T and T_{rad}. (b) Same as panel (a), multiplied by $2\mathrm{Ro}_T$. In both panels, the hatched region marks simulations for which $\overline{u_1}$ switches sign more than 10% of the time in the last 700 rotation periods of the simulation. The thick black line marks the transition from superrotation to subrotation. In panel (b), filled symbols show approximate parameters for known tidally locked terrestrial planets: GJ1132b (square), LHS 1140 b (cross), Trappist 1b (plus sign), Trappist 1 c (diamond), Trappist 1d (circle), 55 Cancri e (downward-pointing triangle), Kepler 10b (upward-pointing triangle). Open symbols show approximate parameters for known hot Jupiters: HD 189733b (squares), HD 209458b (cross), HD 149026b (plus sign), HAT-P-7b (diamond), WASP-18b (circle), WASP-12b (downward-pointing triangle). Planets that fall outside of the regime diagram are brought to the nearest value; arrows are used to indicate planets for which $T_{\mathrm{rad}} < 5$ or $\mathrm{Ro}_T > 20$. See Appendix D for details on the parameters and estimation.

Various observed tidally locked terrestrial planets and gas giants are featured in Figure 5(b). The uncertainty of the positioning can be large, especially on T_{rad} (due to poorly constrained atmospheric depth and composition—see Appendix D for details on the parameter estimation). However, the vast majority do lie in the low-T_{rad} regime owing to the proximity to their host stars, leading to high equilibrium temperatures. As a consequence, all are localized in the superrotating regime.

4.1.2. Low-Ro_T Regime

Spanning two orders of magnitude in each of the two control parameters, our simulations sample very different regimes. We now investigate the behavior of four representative simulations, roughly sitting at each corner of the parameter space. We begin with the low-Ro_T regime, choosing one run with weak thermal inertia ($T_{\mathrm{rad}} = 10$, which superrotates) and one with large thermal inertia ($T_{\mathrm{rad}} = 400$, which subrotates). Figures 6(a) and (d) depict the time-mean state of the upper level.

The low-Ro_T, low-T_{rad} regime has a superrotating equatorial jet and two eastward midlatitude jets, with westward flow in subtropical regions. The combination of low Ro_T, which limits temperature homogenization by gravity waves at low latitudes (R. T. Pierrehumbert & M. Hammond 2019), and low T_{rad}, which imposes strong relaxation toward the forcing temperature profile, yields large temperature gradients. The low-Ro_T, high-T_{rad} regime features a more homogeneous temperature profile owing to the larger thermal relaxation time. Its zonal-mean circulation is somewhat Earth-like, with a retrograde equatorial jet and two eastward midlatitude jets. Both simulations feature Hadley cells (Figures 6(a) and (d), dashed orange lines), with poleward flow extending to about 45° for $T_{\mathrm{rad}} = 10$ and 35° for $T_{\mathrm{rad}} = 400$. Weak reversed cells are present within 10° of the equator at low T_{rad}.

What leads to these very different zonal-mean wind profiles? Our analysis of the Matsuno–Gill model (Section 3.2) suggested that, on tidally locked planets, equatorial EMFC driven by the stationary response to the day–night insolation gradient should decrease with T_{rad}. To verify whether this behavior holds in the fully nonlinear simulations, we separate the contributions from the zonal-mean flow (mean meridional circulation (MMC)), stationary eddies (SEs), and transient eddies (TEs) to the zonal-mean zonal momentum budget of the upper layer. As before, zonal averages and deviations from these are denoted by $\overline{(\cdot)}$ and $(\cdot)'$, respectively. Time averages and deviations from these are denoted by $[\cdot]$ and $(\cdot)^{\dagger}$, respectively. Equation (13) is decomposed as (see J. P. Peixoto & A. H. Oort 1992, Equation (4.9); R. Seager et al. 2003, Equation (1))

$$\left[\overline{\frac{\partial u_1}{\partial t}}\right] = \underbrace{(f + \mathrm{Ro}_T[\overline{\zeta_1}])[\overline{v_1}] - \mathrm{Ro}_T\,[\overline{\omega}]\,[\overline{u_2 - u_1}]}_{\text{MMC}} + \underbrace{\mathrm{Ro}_T(\overline{[\zeta_1]'[v_1]'} - \overline{[\omega]'[u_2 - u_1]'})}_{\text{SE}} + \underbrace{\mathrm{Ro}_T([\overline{\zeta_1^{\dagger} v_1^{\dagger}}] - [\overline{\omega^{\dagger}(u_2 - u_1)^{\dagger}}])}_{\text{TE}}. \quad (30)$$

The left-hand side vanishes in equilibrium. The Matsuno–Gill pattern studied in Section 3.2 is relevant to the behavior of the SE term, while transient waves such as midlatitude Rossby waves or the RK mode of Section 3.3 are relevant to the TE term.

Equation (30) is evaluated in statistical equilibrium in Figures 6(b) and (e). In this low-Ro_T regime, the meridional pattern of SE momentum flux convergence qualitatively resembles that of the Matsuno–Gill model (Figure 3(a)), with three local maxima (two in midlatitudes and one at the equator). The overall magnitude of the SE term and the strength of its equatorial maximum relative to the midlatitude peaks both decrease with T_{rad}, in line with the Matsuno–Gill model. Interestingly, in both cases, the SE term is mostly balanced by TEs close to the equator, with the MMC having a weak contribution there. Similar behavior was previously observed in a GCM with Earth-like parameters (N. J. Lutsko 2018).

To get more insight into the nature of the westward momentum flux at low latitudes, we calculate a spectral decomposition of the transient EMFC (known as a cospectrum; see Appendix E; W. J. Randel & I. M. Held 1991;

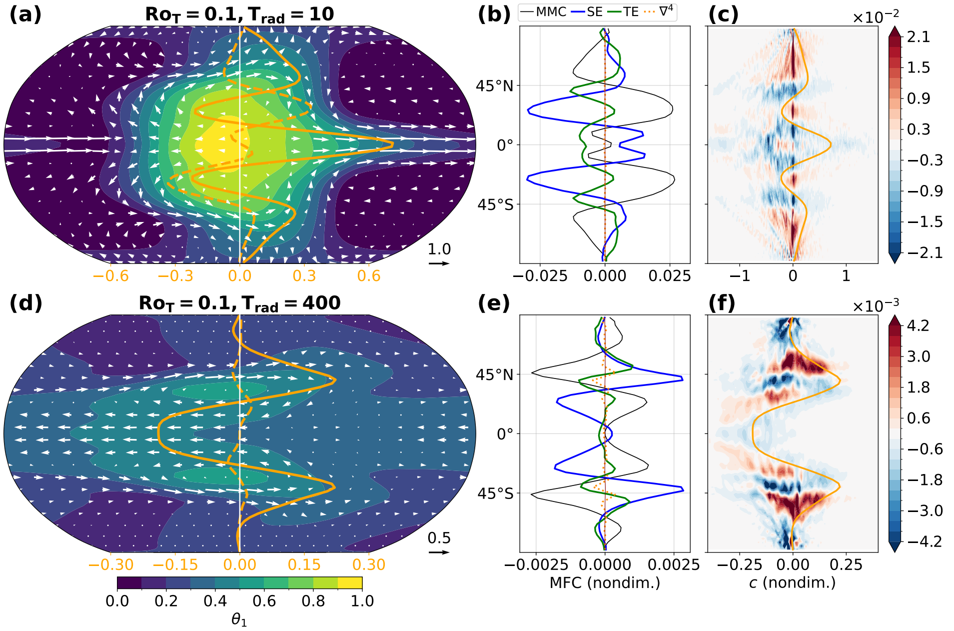

Figure 6. Equilibrium properties of two $\mathrm{Ro}_T = 0.1$ tidally locked simulations, with (a–c) $T_{\mathrm{rad}} = 10$ and (d–f) $T_{\mathrm{rad}} = 400$. (a, d) Mean upper-level potential temperature (shading) and winds (arrows). Orange lines show $[\overline{u_1}]$ (solid) and $[\overline{v_1}]$ (dashed, multiplied by 5 for visibility), with a scale shown at the bottom of each axis. (b, e) Upper-level zonal-mean zonal momentum budget (Equation (30)) in equilibrium. Shown are the contributions of the MMC (black), SEs (blue), TEs (green), and hyperdiffusion (dotted orange). The small residual due to $[\partial_t \overline{u_1}]$ and numerical diffusion in the time-stepping scheme is shown as a thin red line. (c, f) Cospectra of upper-level transient EMFC in (latitude, phase speed) space. See Appendix E for definition. Solid orange lines show $[\overline{u_1}]$; Rossby waves generated at high latitudes preferentially break and deposit westward momentum along these lines.

J. L. Mitchell & G. K. Vallis 2010). Figures 6(c) and (f) show the contribution of eddies of a given phase speed to the TE term at each latitude. Eddies generated at midlatitudes will tend to break and deposit their momentum along their critical line, i.e., where their phase speed equals the zonal-mean zonal wind $\overline{u_1}$ (the critical line is shown in orange in Figures 6(c) and (f)). In the subrotating case (Figure 6(f)), high-latitude eddies converge eastward momentum slightly poleward of the location of the jets and diverge it along the critical line equatorward of it (W. J. Randel & I. M. Held 1991). Close to the equator, eddies of various phase speeds deposit westward momentum, but these are not clearly connected to breaking high-latitude waves. In the superrotating case, the pattern of EMFC around the midlatitude jets is relatively similar, with westward momentum deposition on the equatorward side of the midlatitude jets, but the behavior of low latitudes is very different, with contributions from eddies of much larger phase speeds.

In summary, the low-Ro_T tidally locked runs can broadly be classified into two categories: a superrotating one at low T_{rad}, and a subrotating one at high T_{rad} (the boundary being at $T_{\mathrm{rad}} \simeq 150$; see Figure 5). Momentum flux convergence by SEs behaves in a qualitatively similar way to the Matsuno–Gill model, providing increasingly weaker eastward equatorial acceleration as T_{rad} increases, and is balanced there by westward acceleration due to TEs. The Hadley circulation has a weak contribution to the zonal momentum balance in the equatorial zone.

4.1.3. High-Ro_T Regime

The other end of the parameter space is illustrated in Figure 7 with two $\mathrm{Ro}_T = 10$ simulations. We choose two superrotating cases, with low and high T_{rad}. Both cases have much more homogeneous temperature distributions than their low-Ro_T counterparts (notice the difference in color scales between Figures 6(a) and (d) and Figures 7(a) and (d)), due to efficient temperature smoothing by gravity waves (D. Perez-Becker & A. P. Showman 2013). The $T_{\mathrm{rad}} = 10$ case features a broad superrotating equatorial jet and westward flow at high latitudes. The $T_{\mathrm{rad}} = 250$ case has planetary-wide eastward flow. This configuration appears in GCMs but cannot occur in 1.5-layer shallow-water models, as some local retrograde flow is required at the equator to allow for vertical transport of eastward momentum in these models, as discussed in the introduction. Hadley cells extend all the way to the poles in both simulations (Figures 6(a) and (d), dashed orange lines).

The zonal-mean zonal momentum budget (Equation (30)) is shown in Figures 7(b) and (e). The Hadley circulation decelerates the equatorial flow, as its ascending branch imports air with lower angular momentum from the lower level. However, this contribution remains weaker than that of SEs and TEs. In this high-Ro_T regime, the SE momentum flux convergence patterns strongly differ from the Matsuno–Gill model: there is only one maximum, at the equator, converging eastward momentum in a broad region. This is because the Matsuno–Gill model assumes no mean flow, while the mean flow strongly influences the shape of SEs at high Ro_T (M. Hammond & R. T. Pierrehumbert 2018).

As in the low-Ro_T regime, most of the SE term is balanced by TEs. This is somewhat surprising in light of the findings of M. Hammond et al. (2020), which showed that in GCM simulations at high Ro_T the SE term was balanced by the vertical part of the MMC term, with TEs being weak. The two-level simulations presented here exhibit stronger time variability than classical GCMs: while T. D. Komacek & A. P. Showman (2019) reported time variability in global mean temperature and wind speed of around 0.1%–1% and 1%–10%, respectively, these figures are 0.3%–15% and

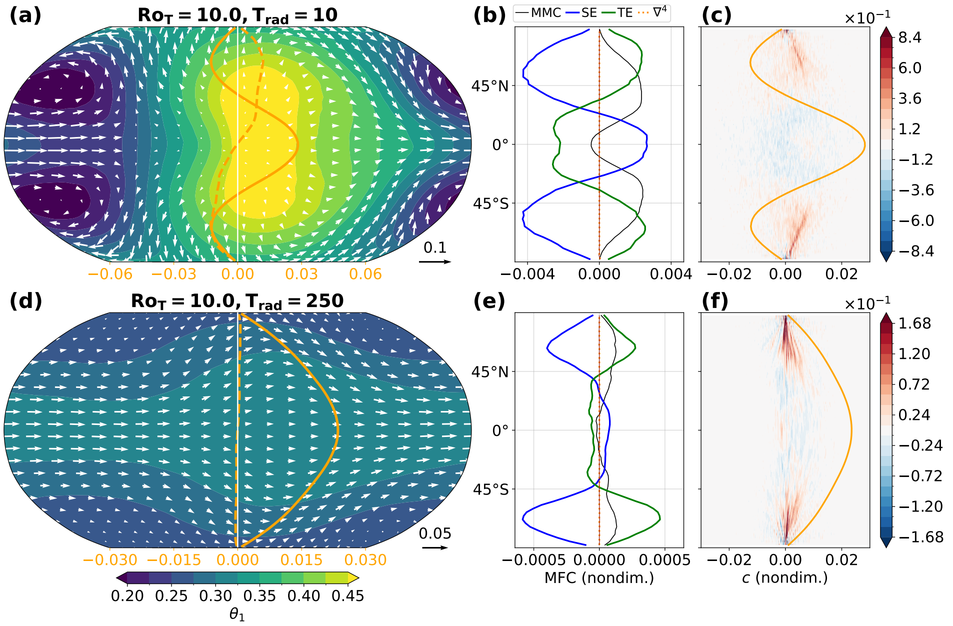

Figure 7. Same as Figure 6, but for two simulations with $\mathrm{Ro}_T = 10$ and $T_{\mathrm{rad}} = 10$ and 250.

10%–40% for $\mathrm{Ro}_T \in [1, 10]$ and $T_{\mathrm{rad}} \in [10, 1000]$ in the two-level model. One factor affecting the strength of the MMC term is the lower-layer drag: simulations with increased drag result in larger zonal-mean vertical shear $\overline{[u_2 - u_1]}$ and hence a larger MMC term (not shown). However, even with $E = 0.2$, the TE term remains of comparable strength to the MMC term. This pattern of strong transients and weak MMC may also arise from the strong vertical truncation inherent to the two-level model or the weak stratification of our relaxation temperature profile and will be explored in a future study.

Eastward EMFC at high latitudes mostly results from eddies of weak positive phase speeds. A broad spectrum of waves contributes to westward EMFC at low latitudes, although isolated signals of eastward acceleration are detectable (in the $T_{\mathrm{rad}} = 250$ case, the most prominent one is related to the mixed Rossby-gravity (MRG) wave, a type of antisymmetric equatorial wave (G. K. Vallis 2017), further discussed in Section 5).

These results do not provide full insights into why the propensity to superrotate increases at high Ro_T (Figure 5), while our quasi-linear analysis of the Matsuno–Gill model seemed to suggest the opposite. We noted above that the analysis of Section 3.2 relied on a resting basic state, whereas the importance of advection by the background wind increases with Ro_T. In particular, P. Barpanda et al. (2023) showed that the presence of meridional shear can lead to a stronger Kelvin wave response than with a resting basic state, which should result in stronger equatorial EMFC. Thus, a basic-state zonal wind such as that shown in Figure 6(d) could, at higher Ro_T, result in a stronger stationary EMFC and thereby switch to a superrotating state. The next section explores another possible answer based on the behavior of TEs.

4.1.4. Propagating Rossby–Kelvin Modes May Contribute to Superrotation Onset at High $\mathrm{Ro_T}$

In this section we show evidence that RK modes exist in some tidally locked simulations (despite being previously studied mainly in the context of slow rotators) and may favor superrotation at high Ro_T. For brevity, we choose the $\mathrm{Ro}_T = 10$, $T_{\mathrm{rad}} = 250$ run analyzed above. However, several simulations (mostly those lying close to the transition between superrotation and subrotation, for $\mathrm{Ro}_T > 1$) exhibit similar behavior.

We start by quantifying the presence of $k = 1$ waves within the RK wave frequency band at the equator. More precisely, we form a time series by taking the $k = 1$ Fourier component of the 30°S–30°N averaged zonal wind. We perform a continuous wavelet transform (C. Torrence & G. P. Compo 1998) on this time series,[6] and we average the power for $\omega \in [0.2, 0.25]$ (motivated by the results of Section 3.3). The result is shown as green lines in Figure 8(a), alongside a time series of the equatorial zonal-mean zonal wind.

The simulation switches from subrotation to superrotation around $t = 2000$, with relatively stable zonal-mean equatorial winds before and after the regime change. The switch is preceded by a burst in wavenumber 1 equatorial wave activity in the RK frequency band. This activity mostly disappears once superrotation has emerged, although a weak burst around $t = 12{,}000$ coincides with a temporary weakening of the equatorial winds. This behavior was observed in a GCM by P. Zurita-Gotor et al. (2022) and is consistent with the fact that the RK mode requires weak equatorial winds for the coupling between the equatorial Kelvin wave and the midlatitude Rossby waves to occur.

We evaluate the spatial structure of this signal by filtering upper-layer geopotential and winds for $t \in [0, 2000]$ for zonal wavenumber $k = 1$ and $\omega = 0.243$ (the frequency that has the strongest contribution to eastward EMFC at the equator for $k = 1$). The resulting pattern (Figure 8(b)) features a clear RK mode structure, with a low-latitude Kelvin wave coupling to midlatitude Rossby waves in a similar fashion to Figure 4.

Finally, we evaluate the contribution of the RK mode to low-latitude EMFC during the spin-up period ($t \in [0, 2000]$). This is done by means of the spectral decomposition outlined in Appendix E: we average the contribution of $k = 1$ waves

---

[6] We use Morlet wavelets with frequencies of the form $2^{-j/12}/(2\pi)$, where j is a nonnegative integer.

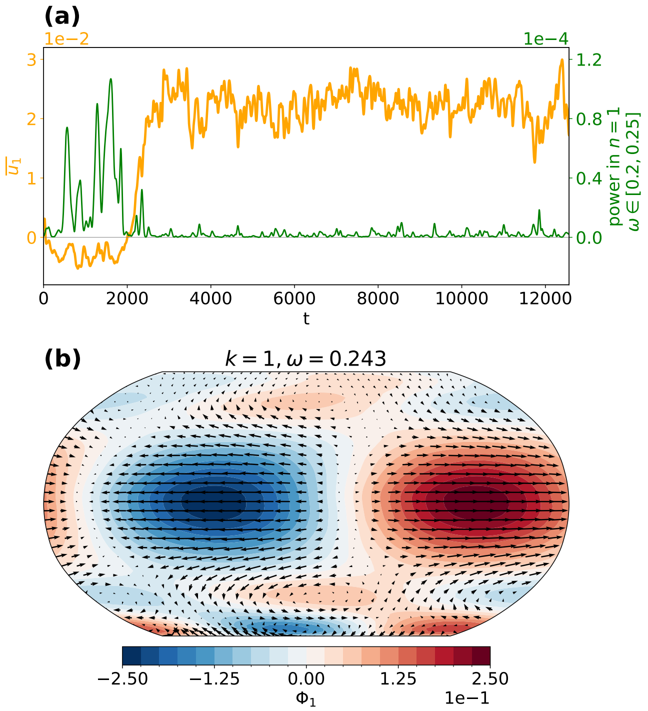

Figure 8. RK mode in a high-Ro_T tidally locked simulation ($\mathrm{Ro}_T = 10$, $T_{\mathrm{rad}} = 250$). (a) Time series of equatorial RK mode power, as measured as the power contained in the [0.2, 0.25] frequency band of the $k = 1$ equatorial zonal wind (green line), along with time series of the equatorial zonal-mean zonal wind (orange line). Both time series are smoothed with a Gaussian filter with standard deviation 4π (1 rotation period). (b) Upper-layer geopotential and winds filtered for $k = 1$ and $\omega = \omega_{\max}$, where $\omega_{\max}$ is the frequency that has maximal EMFC contribution over 30°S–30°N for $t \leqslant 2000$ (see text).

(i.e., $K_{1,\omega}(\phi)$; see Equation (E4)) over the RK mode frequency band, taken as $\omega = [0.2, 0.25]$. The mode has positive EMFC between 30°S and 30°N (not shown; roughly the extent of the Kelvin wave in Figure 8(b)), averaging 1.5×10^{-5}. In comparison, the stationary EMFC (SE term in Equation (30)) is positive between 15°S and 15°N and averages 7.5×10^{-5} over that same period. The RK mode thus has a weaker but important contribution to the acceleration of superrotation.

This result suggests that an RK instability may contribute to the transition to superrotation even in some classes of tidally locked planets, specifically for $\mathrm{Ro}_T \gtrsim 1$. This is consistent with the findings of H. Innes & R. T. Pierrehumbert (2022) for sub-Neptunes, which are in a very high Ro_T regime ($\mathcal{O}(10\text{–}10^3)$). The presence of the instability may be favored by the weakness of the Matsuno–Gill response in that regime (Section 3.2), as well as the relative axial symmetry of the basic-state flow (Figure 7(d)).

4.1.5. Importance of Low-level Drag

One important prediction from the quasi-linear solutions of Section 3.2 is that the Matsuno–Gill pattern does not accelerate superrotation in the absence of low-level drag. To test whether this affects the appearance of superrotation in fully nonlinear runs, we rerun three simulations with $E = 0$ (i.e., we switch off Rayleigh drag altogether). We choose to fix $T_{\mathrm{rad}} = 40$ (a value at which all simulations superrotate with our reference value of $E = 0.02$) and use three values of Ro_T: 0.1, 1, and 10.

The equilibrium $\overline{u_1}$ is shown in Figure 9 for our control runs (solid) and no-drag runs (dashed). Shutting off low-level drag removes superrotation in the $\mathrm{Ro}_T = 0.1$ and $\mathrm{Ro}_T = 1$ runs, consistent with the Matsuno–Gill model behavior. In the $\mathrm{Ro}_T = 10$ case, however, the superrotating jet is only slightly weakened by the removal of drag. This confirms our previous conclusion that the Matsuno–Gill model is more relevant at low Ro_T. It is also consistent with our finding that RK instability is linked to the appearance of superrotation at high Ro_T: indeed, RK modes do not require surface drag to produce equatorial EMFC (Section 3.3).

The comparison with shallow-water models deserves a comment. 1.5-layer shallow-water models such as in A. P. Showman & L. M. Polvani (2011) prescribe drag in the upper layer and have essentially infinite drag in the lower layer. Thus, "drag-free" solutions of such models are not comparable to the present two-level runs, because they are only drag-free in the upper layer (as are all runs presented in the present work)—they do, in fact, superrotate.

Finally, we test the sensitivity to increased low-level drag and run the same three simulations with $E = 0.2$. This value is 10 times higher than our reference choice and corresponds to a timescale of 0.4 rotation periods; it is thus on the upper end of drag values typically used in GCM studies of tidally locked planets (B. Liu & A. P. Showman 2013). Stronger drag results in stronger superrotating jets in all three cases, with a clear regime shift in the $\mathrm{Ro}_T = 1$ case from three jets to a single equatorial jet. This is consistent with the Matsuno–Gill pattern still being relevant in the appearance of superrotation at $\mathrm{Ro}_T = 1$.

4.2. Axisymmetrically Forced Planets, or "Slow Rotators"

To model superrotation in axisymmetrically forced planets, we use the same setup and set of parameters as in Section 4.1, except that the equilibrium potential temperature profiles are now zonally symmetric—see Equation (6). Each run is integrated for 500 rotation periods (ample to reach statistical equilibration), with averaged values taken over the last 350 periods. Our main goal is to isolate the mechanism of any superrotation and to see whether and how it is tied to RK instability as the flow becomes nonlinear.

Figure 10(a) displays a regime diagram of the equilibrium equatorial jet speed in the upper level, in (Ro_T, T_{rad}) space. Most of these axisymmetrically forced planets subrotate. Consistent with previous studies (e.g., S. F. Potter et al. 2014), superrotation is favored at high Ro_T (here $\mathrm{Ro}_T \gtrsim 1.5$), albeit only when T_{rad} is within certain bounds. The Ro_T threshold for superrotation is similar to previous studies (J. L. Mitchell & G. K. Vallis 2010; S. F. Potter et al. 2014), and the low-T_{rad} cutoff was previously observed in a GCM by J. R. Dias Pinto & J. L. Mitchell (2014). As in the tidally locked cases, the boundary between subrotation and superrotation is not well-defined in all parts of the parameter space: some simulations, especially at high Ro_T and low T_{rad}, oscillate between both states even in statistical equilibrium. Somewhat surprisingly, a second region of the phase space, specifically at low Ro_T and low T_{rad}, superrotates. While we do not focus on this case, preliminary examination suggests that high-wavenumber MRG waves accelerate superrotation in that regime. Finally, as in the tidally locked case, the equatorial jet speed strengthens with Ro_T when measured as a fraction of the planetary angular momentum (Figure 10(b)). Earth and Mars are clearly in the subrotating regime of this diagram. Titan has both high Ro_T and high T_{rad} (Appendix D) and thus lies outside of the parameter range explored here.

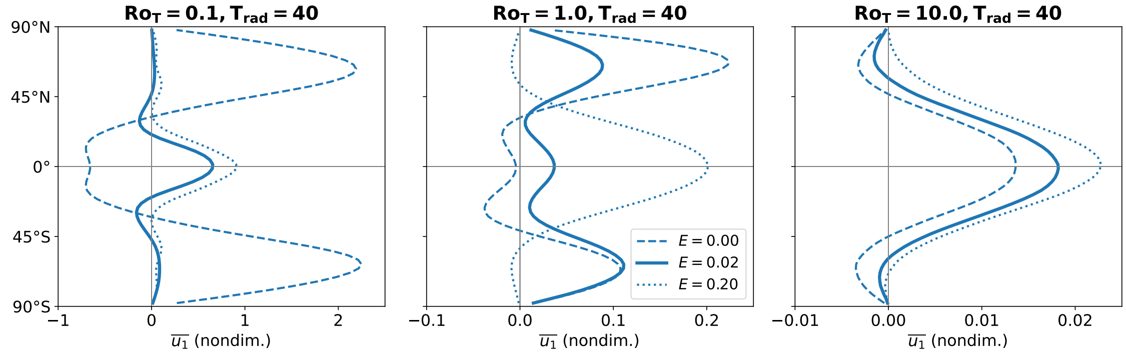

Figure 9. Upper-level zonal-mean zonal wind in two-level runs with no drag (dashed lines), our reference drag value (solid lines, corresponding to damping time of 4 rotation periods), and strong drag (dotted lines, corresponding to a damping time of 0.4 rotation periods).

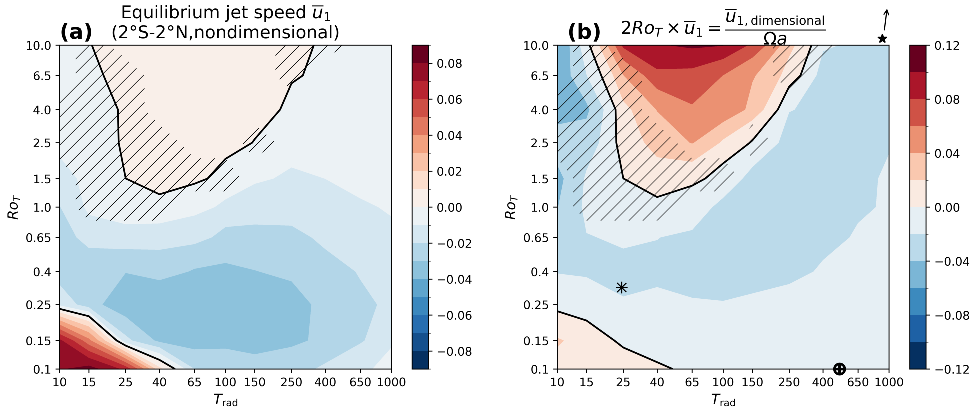

Figure 10. Same as Figure 5, but for axisymmetrically forced planets. The locations of Earth (⊕) and Mars (*) are indicated; Titan (⋆) lies outside of the regime diagram (see Appendix D).

Can the superrotation be linked to RK instability at high Ro_T? We provide evidence for this on one example ($\mathrm{Ro}_T = 10$, $T_{\mathrm{rad}} = 25$), although all superrotating simulations with $\mathrm{Ro}_T \geqslant 0.5$ behave in a similar fashion. We analyze the equilibrated state ($t \geqslant 300$ days), but results including the spin-up time are very similar. The cospectrum of EMFC in the upper layer (Figure 11(a)) shows a clear signal at all latitudes corresponding to a frequency of 0.23 and wavenumber $k = 1$. This wave contributes most of the eastward acceleration at the equator. The upper-layer geopotential and winds are filtered for this exact frequency and wavenumber (Figure 11(b)), and they show a classical RK pattern, similar to Figure 4(a), flanked by a set of high-latitude Rossby waves close to each pole. While the case presented in Figure 11 has relatively simple behavior, the cospectra of other superrotating simulations can have more complex structures (not shown). The footprint of RK modes is present in all of them, but other types of waves, particularly a $k = 2$ westward-traveling MRG wave (further discussed in Section 5), contribute to superrotation in some cases (echoing the results of N. T. Lewis et al. 2023).

As explained in Section 3.3, the existence of unstable RK modes requires two conditions: a Froude number $\mathrm{Fr} \geqslant 1$ and sufficient physical overlap between the waves, as measured by the ratio L_d/ϕ_0. The values of Fr and L_d/ϕ_0 are shown in the parameter space of the simulations in Figure 12(a). A basic-state wind $U(\phi)$ is obtained by averaging $(u_1 + u_2)/2$ over both hemispheres, and ϕ_0 is taken as the latitude where U maximizes. Fr is calculated as $\mathrm{Fr} = [U(\phi_0)/\cos\phi_0]/(U_{\mathrm{eq}} + c)$ to take into account Doppler-shifting of the equatorial Kelvin wave by the mean flow (c is given by Equation (29)), with U_{eq} averaged between 30°S and 30°N. The stratification in c is taken as the difference $\theta_1 - \theta_2$ averaged over the same equatorial band. Fr turns out to be larger than 1 over much of the parameter space, indicating that the midlatitude jets are fast enough for Rossby waves to phase-lock with equatorial Kelvin waves, except at low Ro_T and high T_{rad} (e.g., for Earth-like planets).

Figure 12(b) shows that the spatial overlap between Rossby and Kelvin waves increases with Ro_T. Except for the low-Ro_T, low-T_{rad} regime, superrotation appears for $L_d/\phi_0 \gtrsim 0.18$ (a lower value than the threshold of 0.3 found with the specific setup of Section 3.3). We observed (not shown) that RK modes are present in all of the simulations that meet both this criterion and $\mathrm{Fr} \geqslant 1$. This condition is not, however, sufficient for superrotation. Examination of the EMFC cospectra in subrotating simulations that meet both criteria shows that they do feature RK modes, but they are generally too weak compared to the westward acceleration provided by the mean flow and other TEs. In the low-T_{rad} regime, this likely happens as the strong thermal damping significantly weakens the RK modes.

P. Wang & J. L. Mitchell (2014) discussed the existence of RK instability in terms of two parameters: the Froude number Fr, and a midlatitude Rossby number $\mathrm{Ro}(\phi_0)$ ($=\mathrm{Ro}_T U(\phi_0)$ with our nondimensional scales). They found that the growth rate of RK modes was an increasing function of the latter, with positive growth rates for $\mathrm{Ro}(\phi_0) \geqslant 0.1$, although they did not provide a physical explanation for this criterion. We nevertheless show the values of $\mathrm{Ro}(\phi_0)$ in Figure 12(c), as it appears

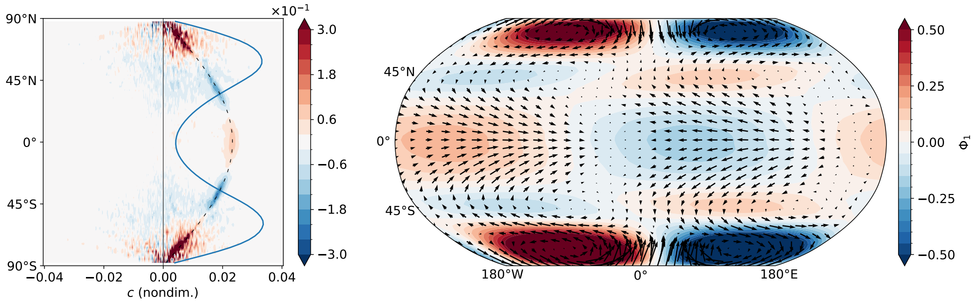

Figure 11. Evidence that RK modes accelerate superrotation in a nonlinear axisymmetrically forced run with $\mathrm{Ro}_T = 10$ and $T_{\mathrm{rad}} = 25$. Left: cospectrum of upper-level EMFC in (latitude, phase speed) space. The solid blue line shows the upper-level zonal-mean zonal wind. The dashed black line shows the phase speed associated with a constant frequency $\omega = 0.23$ and wavenumber $k = 1$. Right: upper-level zonal geopotential (shading) and zonal wind (arrows) filtered for $k = 1$ and $\omega = 0.23$.

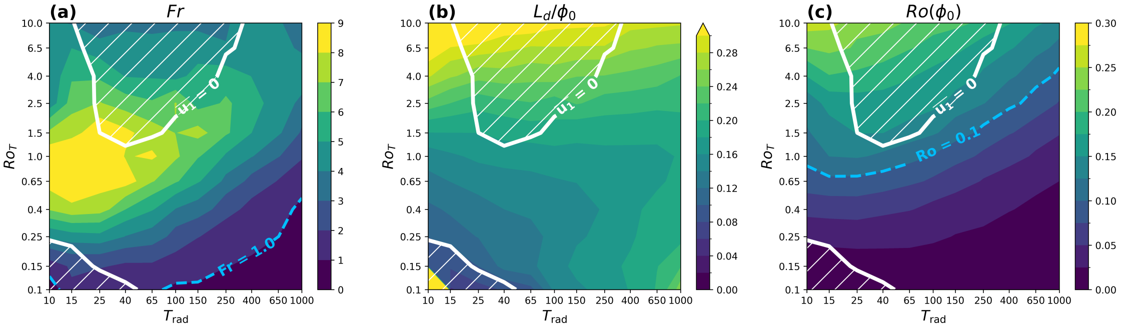

Figure 12. Diagnostics for the existence of RK instability in the suite of axisymmetrically forced simulations. Shading shows (a) Froude number, (b) ratio of the equatorial Rossby deformation radius to the latitude of maximum zonal wind speed, and (c) Rossby number at the latitude of maximum zonal wind speed. Dotted blue lines in panels (a) and (c) indicate the lower bounds for RK instability from P. Wang & J. L. Mitchell (2014). The hatched regions enclosed by solid white contours delineate the regions of the (Ro_T, T_{rad}) phase space that superrotate.

that $\mathrm{Ro}(\phi_0) \gtrsim 0.12$ is the best-fitting criterion for the existence of superrotation in our simulations. Further study is needed to understand why $\mathrm{Ro}(\phi_0)$ is a better control on superrotation than the physical overlap of Rossby and Kelvin waves, as measured by L_d/ϕ_0.

4.3. Interpretation of Nonlinear Results

Nonlinear, time-dependent simulations in both tidally locked and axisymmetrically forced planets show results that are broadly consistent with the quasi-linear analysis but have various quantitative differences. In the tidally locked case at low Ro_T the momentum flux is similar to that expected from a Matsuno–Gill pattern, giving superrotation when thermal damping is strong but with nonlinear, TE effects damping superrotation if thermal damping is weak. At higher Rossby number (slower rotation) the patterns arising in the nonlinear simulations diverge more from the linear Matsuno–Gill pattern, largely because of the effect of advection of the pattern by the mean flow that is itself induced by the eddies (evidently a nonlinear effect), and fluxes from TEs become important. Superrotation then arises over a broad range of T_{rad} values.

In the axisymmetric model, superrotation exists in two regions of parameter space: low Ro_T/low T_{rad}, and $\mathrm{Ro}_T \geqslant 1$ with medium values of T_{rad}. In the latter case, RK modes are a necessary (but not always sufficient) condition for the appearance of superrotation: they do, by and large, produce eddy momentum fluxes that lead to superrotation, as the quasi-linear results suggest (e.g., as in Figure 11). Criteria based on the phase speed ratios and the spatial overlap between midlatitude Rossby waves and equatorial Kelvin waves help characterize in which parts of the parameter range these modes are present.

5. Transition from a Slow Rotator to a Tidally Locked Planet

The mechanisms of superrotation on tidally locked and axisymmetrically forced planets both involve a coupling between midlatitude Rossby waves and equatorial Kelvin waves. However, the waves in the tidally locked case are predominantly forced stationary waves, whereas those on axisymmetrically forced planets arise from an instability and have a fast eastward propagation. In this section, we explore the transition between the axisymmetrically forced and tidally locked regimes. Specifically, we fix all parameters and run a suite of simulations where we only vary the longitudinal structure of the thermal forcing, thereby forming a continuum between axisymmetric and tidally locked thermal forcing. Our goal is to understand the interplay between RK waves and stationary waves forced by zonal asymmetries.

All six simulations presented in this section feature $\mathcal{S} = 0.05$, $E = 0.02$, $\mathrm{Ro}_T = 10$, and $T_{\mathrm{rad}} = 250$. We choose these values of Ro_T and T_{rad} because both tidally locked and axisymmetrically forced cases superrotate in this regime, and the tidally locked case also features RK instability during its spin-up phase. The runs only differ in the zonal structure of their thermal forcing. The two end-members were already described in Section 4: one is axisymmetric (i.e., $\theta_{iE} = (1 - \mathcal{S} \ln \Pi_i) \cos\phi \,(1/\pi)$), and the other one is tidally locked (i.e., $\theta_{iE} = (1 - \mathcal{S} \ln \Pi_i) \cos\phi \, \max(0, \cos\lambda)$). Four

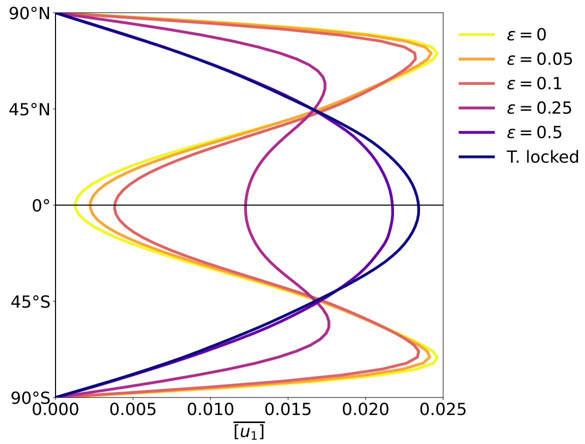

Figure 13. Upper-layer zonal-mean zonal wind in a suite of two-level runs with increasing $k = 1$ heterogeneities in thermal forcing, with $\mathrm{Ro}_T = 10$ and $T_{\mathrm{rad}} = 250$.

runs with increasingly stronger zonal asymmetries bridge these two. Recalling that $\max(0, \cos\lambda)$ expands in Fourier series as $1/\pi + (\cos\lambda)/2 + \ldots$, we define a parameter ϵ such that θ_{iE} is given, in these runs, by

$$\theta_{iE} = (1 - \mathcal{S}\ln\Pi_i)\cos\phi\left(\frac{1}{\pi} + \epsilon\cos\lambda\right), \qquad (31)$$

and we use four values of ϵ: 0.05, 0.1, 0.25, and 0.5. All simulations are run for 1000 rotation periods, with statistical equilibrium reached within 300.

Equilibrated $\overline{u_1}$ profiles (Figure 13) observe a transition from a regime with two strong high-latitude jets and weaker equatorial flow (axisymmetric or weakly zonally asymmetric cases) to a regime where the zonal wind increases monotonously from the poles to the equator ($\epsilon = 0.5$ and tidally locked cases). The jet strength increases with ϵ, showing that SE forcing helps achieve stronger superrotation than RK instability alone. Finally, the $\epsilon = 0.5$ and tidally locked simulations have a very similar profile, indicating that the higher-order harmonics in the zonal structure of the thermal forcing in this tidally locked case only play a weak role.

Figure 14 (top row) shows the zonal-mean zonal momentum budget terms in statistical equilibrium. In all simulations, the MMC accelerates $\overline{u_1}$ westward at the equator, due to the ascending branch of the Hadley circulation advecting weaker angular momentum from the lower layer. In the $\epsilon = 0$ case, the absence of forced zonal heterogeneity mandates that the SE component vanish. Hence, the only term that can balance westward acceleration of the mean flow is that arising from TEs. The bottom row of Figure 14 explores the TE component by way of the spectral decomposition (E3). This quantifies the contribution of each wave of zonal wavenumber k and frequency ω to transient EMFC at each latitude, here averaged over the equatorial band. Several isolated peaks of eastward acceleration stand out, the strongest corresponding to $k = 1$ and $\omega = 0.2$: this is the $k = 1$ RK mode. Higher-order RK modes are also present and are flagged with plus signs on the spectral diagram. Another strong peak, marked with a star, corresponds to a $k = 2$ westward-traveling wave; further investigation (not shown) shows that its structure resembles an MRG wave. The mode is almost purely antisymmetric (thus, $\mathrm{EMFC}_1 \simeq \mathrm{Ro}_T\overline{\zeta_1' v_1'}$), and the winds organize in a bow shape around the equator: regions of northward winds curve cyclonically, and regions of southward winds curve anticyclonically, such that $\overline{\zeta_1' v_1'} > 0$.

As ϵ increases, introducing stationary zonal inhomogeneity, the westward equatorial acceleration resulting from the MMC changes little. However, the stationary component progressively replaces TEs in providing eastward acceleration, until the TE component switches sign between $\epsilon = 0.1$ and $\epsilon = 0.25$. RK modes are present in statistical equilibrium for $\epsilon \leqslant 0.1$. Beyond that, the equatorial flow strengthens significantly (Figure 13), so that the Froude number is too small for RK modes to persist. While this may suggest that SEs are the sole driver of superrotation for $\epsilon \geqslant 0.25$, TEs are still found to play a prominent role. Indeed, RK modes are observed during the spin-up phases of the $\epsilon \geqslant 0.25$ and tidally locked simulations (shown for the latter in Figure 8). MRG waves also persist in these simulations (Figure 14) and have a strong contribution toward eastward equatorial acceleration. Westward acceleration is primarily the result of low-frequency wavenumber 1 eddies, which are present in all simulations and strengthen with ϵ.

The simulations of M. J. Suarez & D. G. Duffy (1992) and R. Saravanan (1993) bear some comparison to those here. Using a similar two-level model but with Earth-like parameters (i.e., $\mathrm{Ro}_T \simeq 0.1$, so relatively quickly rotating), they studied the effect of increasing the strength of stationary $k = 2$ thermal forcing at the equator. They observed a sudden switch from subrotation to superrotation that seemed primarily driven by the behavior of TEs. I. Kraucunas & D. L. Hartmann (2005) argued that some of this behavior was not robust, as similar experiments in more vertically resolved GCMs showed SEs to have the prominent role. Our simulations actually behave rather similarly to multilevel GCMs, as SE forcing (rather than TE forcing) increases with increasing zonally asymmetric heating. This may also explain why the transition in equatorial winds is not as sudden in our simulations (Figure 13) as those of M. J. Suarez & D. G. Duffy (1992) and R. Saravanan (1993): their mechanism relied on a change in the low-latitude absorption of eddies generated at high latitudes, which has a threshold behavior depending on the equatorial wind speed. While the behavior of our two-level runs is reassuring in that aspect, it does not obviate the necessity of verifying the results in multilevel models.

6. Summary and Discussion

6.1. Summary

In this paper we have explored the presence and mechanisms of superrotation on both tidally locked planets and axisymmetrically forced slow rotators, using one of the simplest models fit for that purpose: a two-level primitive equation model. Four parameters control its behavior: a thermal Rossby number Ro_T, which is higher for small, slowly rotating, or strongly irradiated planets; a nondimensional thermal relaxation timescale T_{rad}, which is a proxy for optical thickness; an Ekman number E parameterizing surface drag; and a nondimensional thermal stratification $\mathcal{S}$. The emphasis is placed on the behavior of superrotation as a function of the first two, although there is some dependence on E.

The steady linear response to the day–night insolation contrast on tidally locked planets, similar to that of the Matsuno–Gill model, provides the basic organizing structure for the eddy effects. However, a Matsuno–Gill pattern of itself,

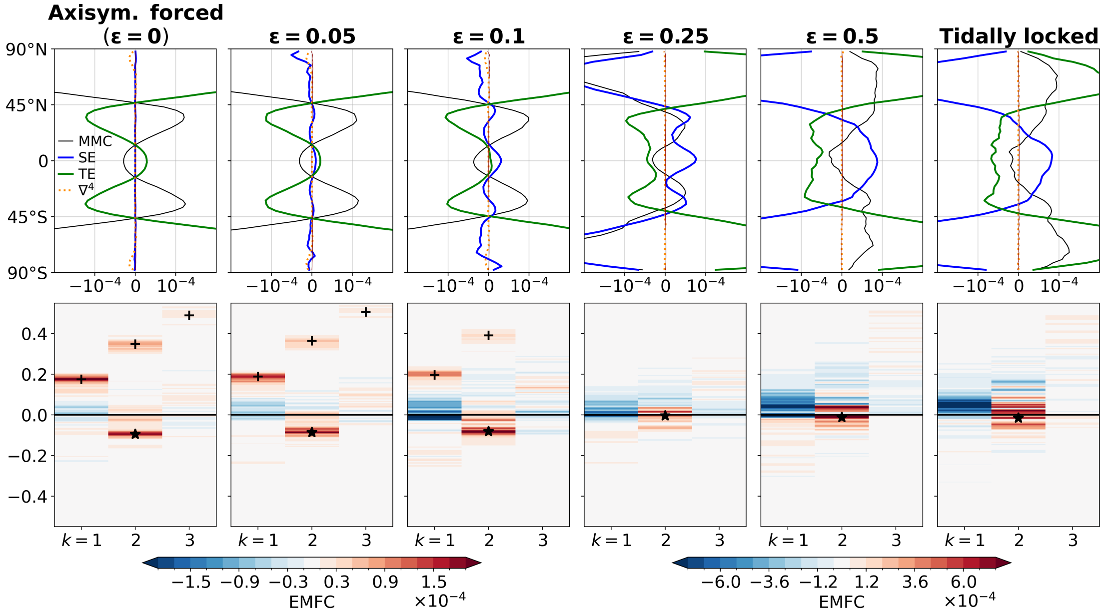

Figure 14. Contributions to the zonal-mean zonal momentum balance in the suite of two-level runs with increasing $k = 1$ heterogeneities in thermal forcing. Top row: zonal-mean zonal momentum balance (30), as in Figures 6(b) and (e). Bottom row: spectral decomposition of the EMFC due to transients $K_{k,\omega}(\phi)$ (see text and Appendix E), averaged for $\phi \in$ [10°S, 10°N]. Plus signs indicate RK modes, and stars indicate westward-propagating MRG-like waves. Gaussian smoothing with standard deviation 5×10^{-3} is applied along the frequency axis. Note that the color scale of the left three panels differs from that of the right three panels by a factor 4.

in a single-layer model, is insufficient to produce superrotation, and both surface drag and vertical structure (to allow for vertical fluxes of momentum) are needed. In the presence of surface drag the strength of the EMFC is a decreasing function (both in absolute terms and relative to midlatitude EMFC peaks) of both Ro_T and T_{rad}. That is, slower rotation and a thicker atmosphere both inhibit superrotation, insofar as the quasi-liner results are relevant.

In slowly rotating axisymmetrically forced planets, unstable RK modes that qualitatively resemble the Matsuno–Gill pattern, similar to those previously identified in GCMs and shallow-water models, also produce superrotation, again provided that some vertical structure is present. Slow rotation is necessary because, without it, the Rossby and Kelvin waves are physically more separated and thus less likely to interact. Unlike the tidally locked case, surface drag is no longer strictly necessary to produce superrotation.

Fully nonlinear integrations reveal very rich behavior. Consistent with the quasi-linear results from the Matsuno–Gill structure, superrotation in tidally locked planets is less favored, as Ro_T and T_{rad} increase when $\mathrm{Ro}_T \leqslant 1$. However, at higher levels of nonlinearity the dependence on Ro_T switches, likely due to the influence of the mean flow on the stationary wave response. The RK modes, generally thought to be more relevant in the context of axisymmetrically forced planets, sometimes arise during the spin-up of superrotation, even in tidally locked planets. A broad class of tidally locked planets with high T_{rad} (i.e., a thicker atmosphere) subrotate; the propensity to subrotate also increases when surface drag is removed, although only for $\mathrm{Ro}_T \leqslant 1$. Thus, although the structure of the eddies is set by the directly forced Matsuno–Gill pattern, transients play a major role in setting the equilibrated state of most tidally locked runs.

In axisymmetrically forced planets, superrotation mainly appears for $\mathrm{Ro}_T \geqslant 1$, i.e., for slow rotators. The factor that limits its appearance is the spatial overlap between equatorial Kelvin waves and midlatitude Rossby waves. If the midlatitude jets are too far poleward or the Kelvin waves too equatorially confined, the overlap is too weak to produce superrotation. In addition, superrotation is inhibited if the midlatitude jets produce Rossby waves that propagate and break in equatorial regions, a phenomenon that seems likely to occur on more Earth-like planets when Ro_T is small.

We finally presented a continuum of simulations bridging axisymmetrically forced and tidally locked states by applying progressively stronger wavenumber 1 thermal forcing, in a regime where RK modes (and superrotation) are present in the two end-members. In spite of a seemingly continuous transition in wind patterns when transitioning from an axisymmetrically forced to a tidally locked planet, the processes responsible for superrotation switch quickly when weak zonal asymmetries are applied. Specifically, a stationary Matsuno–Gill-like pattern soon dwarfs the contribution from propagating waves in setting the total eddy momentum fluxes. However, the two processes can and do coexist, and some of the unstable modes from the axisymmetric case may still be present when strong zonal asymmetries are applied. RK modes are present in the spin-up phases of all cases, but they are only present in the equilibrated state for weak zonal inhomogeneity in the forcing.

6.2. Comparison to Other Models

The two-level model is envisioned as a step of intermediate complexity between 1.5-layer shallow-water models, such as that of A. P. Showman & L. M. Polvani (2011), and GCMs. Unlike 1.5-layer shallow-water models, the two-level model is able to produce superrotation on slow rotators, as well as superrotation at all longitudes on tidally locked planets. It also contains baroclinic instability, a process mostly absent in 1.5-layer shallow-water models but that can impede superrotation. These differences come from the fact that the two-level model has a moving lower layer (whereas 1.5-layer shallow-water models take it to be quiescent) and a different treatment of the vertical momentum advection ($\omega(\boldsymbol{u}_2 - \boldsymbol{u}_1)$ in the two-level model vs. the $\boldsymbol{R}$ term in A. P. Showman & L. M. Polvani 2011). A downside is that analytical treatment of the Matsuno–Gill response is more complex in the two-level model.

We acknowledge several limitations of the model. The strong vertical truncation may misrepresent vertical momentum transport by the eddies and the mean flow alike (as suggested, e.g., by the large time variability described in Section 4.1.3); future work will explore whether the mechanisms described here hold when the vertical structure is better resolved. The present study also misses a realistic treatment of atmospheric composition and radiation, which would directly influence the stratification $\mathcal{S}$ and cooling timescale T_{rad}, likely leading to spatial variations in these. We also neglected the diurnal cycle of insolation on slow rotators, thereby leaving out the potentially important effect of thermal tides at low T_{rad}. Finally, condensible species are not represented here but may have wide-ranging effects, such as influencing planetary albedo (J. Yang et al. 2013; J. Yang & D. S. Abbot 2014), increasing dayside stratification (T. M. Merlis & T. Schneider 2010), and influencing stationary waves through latent heat release or cloud radiative effects (e.g., M. Cohen et al. 2023).

6.3. Implications for Superrotation in Observations

Overall, it may be fairly said that the mechanisms of superrotation in slowly rotating planets are becoming well established, with an RK instability involving both horizontal and vertical eddy momentum fluxes playing a role. The (admittedly limited) observations of slow rotators in the solar system are generally supportive of the mechanisms identified in this paper and by previous investigators (e.g., S. Iga & Y. Matsuda 2005; J. L. Mitchell & G. K. Vallis 2010; P. Wang & J. L. Mitchell 2014; P. Zurita-Gotor & I. M. Held 2018). Tidally locked planets present a different challenge because, although there are many examples, detailed observations are sparse and will remain so, even with JWST. Our results suggest that superrotation on such planets is common but not universal. The importance of drag at the base of the moving atmosphere suggests that the interaction of the shallow atmosphere (i.e., that driven by stellar irradiation) with the deeper atmosphere deserves further investigation, for the mechanisms producing such a drag are not obvious.

The rather general conditions favoring superrotation are a large thermal Rossby number, favored by a slow rotation and smaller planet, and a smaller thermal relaxation timescale, corresponding to a thin atmosphere (see, e.g., Figure 5). As noted, the presence of a mechanical drag also tends to favor superrotation, suggesting that, if all else is equal, a planet with an atmosphere above a rocky surface is more likely to superrotate than a gas giant that may have less drag.

Although winds on exoplanets have been directly measured (e.g., M. Brogi et al. 2016), measurements of phase curves and hot spot offset are more common and the degree of offset does not necessarily correspond to the degree of superrotation. In particular, thin atmospheres that relax quickly back to a thermal equilibrium temperature (a condition generally favoring superrotation) will have less hot spot offset than a similarly superrotating thick atmosphere, as is seen in Figure 7. Given this, independent observations of superrotation and hot spot offset of the same planet could be very revealing about the planet's atmosphere. Further exploring the robustness and observational consequences of our results will be the subject of future work.

Acknowledgments

The authors would like to thank Pablo Zurita-Gotor for many insights that greatly benefited the manuscript, as well as Neil Lewis and an anonymous reviewer for their very helpful comments. They also thank Keaton Burns and Daniel Lecoanet for their help with Dedalus and Jonathan Mitchell and Tad Komacek for useful conversations about superrotation. Both authors were supported by the 2023 WHOI Geophysical Fluid Dynamics Summer Program (funded by the National Science Foundation and the Office of Naval Research), where this project was started. Q.N. was partially supported by an ETH Zürich Postdoctoral fellowship (project No. 24-1 FEL-032) and by the Schweizerischer Nationalfonds zur Förderung der Wissenschaftlichen Forschung (grant No. 219244). For the purpose of open access the authors have applied a Creative Commons Attribution (CC BY) license to any Author Accepted Manuscript version arising from this submission.

Software: Code used to run the Dedalus simulations and code used in producing the figures are archived at Zenodo (doi:10.5281/zenodo.19050783; Q. Nicolas 2026).

Author Contributions

Conceptualization: G. K. Vallis & Q. Nicolas. Investigation: Q. Nicolas. Writing—original draft: Q. Nicolas. Writing—review, editing, and final draft: G. K. Vallis & Q. Nicolas.

Appendix A
Drag-free Solution of the Two-level Matsuno–Gill Problem

We seek a solution of the linear system given by Equations (17a)–(17d) in the case where $E = 0$. The vorticity balance in layer i is

$$f \nabla \cdot \boldsymbol{u}_i' + \beta v_i' = 0. \tag{A1}$$

Combining with continuity, one obtains $v_1' + v_2' = 0$, which also implies $u_1' + u_2' = 0$; hence, $\boldsymbol{u}_1' = -\boldsymbol{u}_2'$. The flow is thus purely baroclinic, and one may show that it satisfies a set of shallow-water equations: Equations (17a)–(17d), along with continuity and hydrostatic balance, yield

$$f\boldsymbol{k} \times (\boldsymbol{u}_1' - \boldsymbol{u}_2') + \nabla(\Phi_1' - \Phi_2') = 0, \tag{A2a}$$

$$\frac{\gamma \mathcal{S} \mathrm{Ro}_T T_{\mathrm{rad}}}{2} \nabla \cdot (\boldsymbol{u}_1' - \boldsymbol{u}_2') + (\Phi_1' - \Phi_2') = \gamma(\theta_{1E}' + \theta_{2E}'), \tag{A2b}$$

which is exactly a single-layer shallow-water system with a gravity wave speed $c_{\mathrm{MG}} = \sqrt{\gamma \mathcal{S} \mathrm{Ro}_T T_{\mathrm{rad}}/2}$, a mass source, and unit damping rate in the thermodynamic equation. The nondimensional equatorial deformation radius in this problem is

$$L_{d,\mathrm{MG}} = \sqrt{\frac{c_{\mathrm{MG}}}{\beta}} = \left(\frac{\gamma \mathcal{S} \mathrm{Ro}_T T_{\mathrm{rad}}}{2}\right)^{1/4}. \tag{A3}$$

A solution to Equations (A2a)–(A2b) can be obtained by first forming a vorticity equation $\nabla \times$ Equation (A2a), yielding

$$f \nabla \cdot (\boldsymbol{u}_1' - \boldsymbol{u}_2') + \beta(v_1' - v_2') = 0, \tag{A4}$$

and combining with the x-momentum equation to obtain

$$\nabla \cdot (\boldsymbol{u}_1' - \boldsymbol{u}_2') = -\frac{\beta}{f^2 \cos\phi}\partial_\lambda(\Phi_1' - \Phi_2'). \tag{A5}$$

Combining Equations (A2b)–(A5) and assuming that each scalar field φ has a structure $\varphi(\phi, \lambda) = \tilde{\varphi}(\phi)e^{ik\lambda}$ ($k = 1$ for the problem considered in Section 3.2), a closed solution for $\Phi_1' - \Phi_2'$ emerges:

$$\tilde{\Phi}_1' - \tilde{\Phi}_2' = \gamma\frac{\tilde{\theta}_{1E}' + \tilde{\theta}_{2E}'}{1 - \frac{ikc_{\mathrm{MG}}^2}{f^2}}. \tag{A6}$$

The wind field can in turn be obtained using Equation (A2a) and $\boldsymbol{u}_1 + \boldsymbol{u}_2 = 0$. The upper-level EMFC is then obtained from the last expression in Equation (14), with $\overline{u_1' v_1'} = \frac{1}{2}\Re(\tilde{u}_1\tilde{v}_1^*)$. A little algebra yields

$$\begin{aligned}&\mathrm{EMFC}_1\\ &= -\mathrm{Ro}_T\kappa\frac{k\gamma^2\xi^2}{8}\frac{Y(Y^3 - 5Y^2 - 7\kappa^2 Y + 3\kappa^2)\sqrt{1 - Y}}{(\kappa^2 + Y^2)^3},\end{aligned} \tag{A7}$$

where $Y = \sin^2\phi$, $\kappa = kc_{\mathrm{MG}}^2$ and $\xi = 1 - S(\ln(\Pi_1) + \ln(\Pi_2)/2 \simeq 1$.

How does the magnitude of EMFC_1 depend on the input parameters $\mathcal{S}$, Ro_T, and T_{rad}, in other words, on κ? When $\kappa \gg 1$, one sees from Equation (A7) that $|\mathrm{EMFC}_1| \propto \mathrm{Ro}_T\kappa\kappa^2/\kappa^6 \propto \mathrm{Ro}_T^{-2}\mathcal{S}^{-3}T_{\mathrm{rad}}^{-3}$. When $\kappa \ll 1$, the maximum of Equation (A7) is attained for $Y \simeq \kappa$, and $|\mathrm{EMFC}_1| \propto \mathrm{Ro}_T\kappa\kappa^3/\kappa^6 = \mathrm{Ro}_T\kappa^{-2} \propto \mathrm{Ro}_T^{-1}\mathcal{S}^{-2}T_{\mathrm{rad}}^{-2}$. With $k = 1$ and $\gamma \simeq 0.12$, the transition between these scalings happens for $\mathcal{S}\mathrm{Ro}_T T_{\mathrm{rad}} \sim 20$: the range of values explored in Section 3.2 is in the low-κ regime.

Last, we provide an expression for the low-level zonal wind u_2 at the equator:

$$u_2(\phi = 0, \lambda) = -\frac{2\xi}{k\mathcal{S}\mathrm{Ro}_T T_{\mathrm{rad}}}\sin(k\lambda). \tag{A8}$$

Appendix B
Eddy Momentum Flux Convergence in the General Two-level Matsuno–Gill Problem

We move away from the simpler drag-free case and seek to obtain a simplified expression for the upper-level EMFC at the equator in the two-level Matsuno–Gill model. As explained in Section 3, $\mathrm{EMFC}_1 = -\mathrm{Ro}_T\overline{\omega'(u_2' - u_1')} = -\mathrm{Ro}_T\overline{\omega' u_2'}$, because $\overline{\omega' u_1'} = 0$ owing to the absence of drag in the upper layer. Using Equations (17c) and (17d) to express ω',

$$-\mathrm{Ro}_T\overline{\omega' u_2'} = \frac{1}{\mathcal{S}T_{\mathrm{rad}}}\overline{(\theta_{1E}' + \theta_{2E}')u_2'} - \frac{1}{\mathcal{S}T_{\mathrm{rad}}}\overline{(\theta_1' + \theta_2')' u_2'}. \tag{B1}$$

We proceed to show that $\overline{(\theta_1' + \theta_2')u_2'} = 0$. Subtracting the upper-layer zonal momentum balance from the lower-layer one at the equator (where $v_1' = v_2' = 0$), one obtains

$$\partial_\lambda(\Phi_2' - \Phi_1') + Eu_2' = 0. \tag{B2}$$

Combining with hydrostasy,

$$-\gamma\partial_\lambda(\theta_1' + \theta_2') + Eu_2' = 0. \tag{B3}$$

Hence,

$$\overline{(\theta_1' + \theta_2')u_2'} \propto \overline{(\theta_1' + \theta_2')\partial_\lambda(\theta_1' + \theta_2')} = 0. \tag{B4}$$

Appendix C
Matsuno–Gill Problem on the Beta Plane

Understanding why the lower-level zonal wind pattern shifts eastward with increased damping is arduous when working with the two-level model, for which no simple analytical solution exists for $E \neq 0$. However, the classical Matsuno–Gill model (i.e., a single-layer model on the beta plane) exhibits the same behavior and is analytically tractable. The model equations are similar to Equations (A2a)–(A2b) with the addition of a mechanical drag of the same strength as the thermal damping (denoted with a coefficient ε). Denoting by $\boldsymbol{u} = (u, v)$ the wind field (which is analogous to $\boldsymbol{u}_2$ or $\boldsymbol{u}_2 - \boldsymbol{u}_1$ in the full two-level model) and Φ the geopotential field (analogous to Φ_2 or $\Phi_2 - \Phi_1$), the model equations are (A. E. Gill 1980; G. K. Vallis 2017, chapter 8.5)

$$\varepsilon u - fv + \partial_x\Phi = 0, \tag{C1a}$$

$$fu + \partial_y\Phi = 0, \tag{C1b}$$

$$\varepsilon\Phi + c^2\nabla \cdot \boldsymbol{u} = -Q, \tag{C1c}$$

where Q is a mass sink, analogous to the heat source in the two-level model. We use a Cartesian coordinate system and make the beta-plane approximation, i.e., we take $f = \beta y$. We also make the long-wave approximation (neglecting friction in the meridional momentum equation, appropriate for the planetary-scale wave considered here). Upon nondimensionalization (details are in G. K. Vallis 2017, chapter 8.5, but are omitted here because only qualitative features of the dependence of u on ε matter), the system can be recast as

$$\varepsilon u - yv/2 + \partial_x\Phi = 0, \tag{C2a}$$

$$yu/2 + \partial_y\Phi = 0, \tag{C2b}$$

$$\varepsilon\Phi + \nabla \cdot \boldsymbol{u} = -Q. \tag{C2c}$$

Solutions are obtained as series expanded in terms of the parabolic cylinder functions $D_n(y)$, $n \in \mathbb{N}$. We shall only need to know the expressions of $D_0(y) = e^{-y^2/4}$ and $D_2(y) = (y^2 - 1)e^{-y^2/4}$. Taking, for simplicity, $Q = Q_0\cos(kx)D_0(y)$, the solution to Equations (C2a)–(C2c) can be expressed as the sum of a Kelvin wave and a Rossby wave. Specifically, the solution is first given in terms of the transformed variables $q = u + \Phi$ and $r = \Phi - u$ and reads as

$$q(x, y) = q_0(x)D_0(y) + q_2(x)D_2(y) \tag{C3a}$$

$$r(x, y) = r_0(x)D_0(y), \tag{C3b}$$

where q_0, q_2, and r_0 verify

$$\partial_x q_0 + \varepsilon q_0 = -Q \tag{C4a}$$

$$\partial_x q_2 - 3\varepsilon q_2 = Q \tag{C4b}$$

$$r_0 = 2q_2. \tag{C4c}$$

The q_0 component represents a forced Kelvin wave, while the q_2 and r_0 components represent a forced Rossby wave. The zonal wind and geopotential perturbations corresponding to each wave are

$$u_{\text{Kelvin}} = \Phi_{\text{Kelvin}} = \frac{q_0(x)D_0(y)}{2} \tag{C5a}$$

$$u_{\text{Rossby}} = \frac{-r_0(x)D_0(y) + q_2(x)D_2(y)}{2} \tag{C5b}$$

$$\Phi_{\text{Rossby}} = \frac{r_0(x)D_0(y) + q_2(x)D_2(y)}{2}. \tag{C5c}$$

In particular, the equatorial zonal wind component carried by each wave is

$$u_{\text{Kelvin}}(x, y = 0) = \frac{q_0(x)}{2} \tag{C6a}$$

$$u_{\text{Rossby}}(x, y = 0) = \frac{-3q_2(x)}{2}. \tag{C6b}$$

In the absence of drag ($\varepsilon = 0$), $q_0 = -q_2$ and both are in quadrature with the forcing Q (in the two-level model, this corresponds to the dashed lines in Figure 3). When drag is added, to first order in ε,

$$u_{\text{Kelvin}}(x, y = 0) = -\frac{1}{2k}\sin(kx) - \frac{\varepsilon}{2k^2}\cos(kx) \tag{C7a}$$

$$u_{\text{Rossby}}(x, y = 0) = -\frac{3}{2k}\sin(kx) + \frac{9\varepsilon}{2k^2}\cos(kx). \tag{C7b}$$

Hence, the Kelvin component shifts westward and the Rossby component shifts eastward. The Rossby component has larger magnitude, and its shift is more pronounced, so the sum shifts eastward with increased drag.

Appendix D
Estimation of Planetary Parameters

The planets shown in Figure 5 are selected following R. T. Pierrehumbert & M. Hammond (2019) and D. Perez-Becker & A. P. Showman (2013). $\Delta\Theta_h$ is taken as the equilibrium temperature T_{eq} of the planet. The specific heat capacity c_p is 10^3 J kg^{-1} K^{-1} for terrestrial planets (assuming a N_2 atmosphere, which is in no way certain; e.g., M. Hammond & R. Pierrehumbert 2017) and 1.2×10^4 J kg^{-1} K^{-1} for hot Jupiters (i.e., assuming a H_2 atmosphere). Following D. Perez-Becker & A. P. Showman (2013), the radiative relaxation timescale is estimated as

$$\tau_{\text{rad}} = \frac{Pc_p}{4g\sigma T_{\text{eq}}^3}, \tag{D1}$$

where σ is is the Stefan–Boltzmann constant and g is the surface gravity. P is the atmospheric depth on tidally locked planets and can be taken at a representative emission level or somewhat deeper for hot Jupiters. We take it as 1 bar in both cases, although there is considerable uncertainty about this figure. Data for terrestrial planets are from R. T. Pierrehumbert & M. Hammond (2019), Q. Xue et al. (2024), C. Cadieux et al. (2024), E. Agol et al. (2021), A. S. Bonomo et al. (2025), and V. Bourrier et al. (2018). All data for hot Jupiters are from K. G. Stassun et al. (2017), except for T_{eq}, which is from D. Perez-Becker & A. P. Showman (2013).

For Figure 10, data for Earth are standard, and τ_{rad} is taken as 40 days (e.g., I. M. Held & M. J. Suarez 1994). For Mars, we use $c_p = 736$ J kg^{-1} K^{-1}, $\tau_{\text{rad}} = 2$ days, and $\Delta\Theta_h = 300$ K (R. M. Haberle et al. 1997). For Titan, we use $c_p = 10^3$ J kg^{-1} K^{-1} and $\Delta\Theta_h = 20$ K (J. L. Mitchell & J. M. Lora 2016). Parameter τ_{rad} is taken as 3×10^8 s (B. Bézard et al. 2018).

All values are summarized in Table 1.

Table 1
Thermal Rossby Number and Nondimensional Radiative Time Constant for Various Tidally Locked Exoplanets and Solar System Planetary Bodies

Planet	Ro_T	T_{rad}
GJ 1132b	1.7	5.6
LHS 1140 b	76	4.5
Trappist 1b	1.2	23
Trappist 1c	2.7	23
Trappist 1d	12	37
55 Cancri e	0.48	0.20
Kepler 10b	1.2	0.19
Planet	Ro_T	T_{rad}
HD 189733b	0.51	9.2
HD 209458b	1.0	7.7
HD 149026b	2.7	3.6
HAT-P-7b	0.52	1.6
WASP-18b	0.16	0.29
WASP-12b	0.10	4.1
Planetary body	Ro_T	T_{rad}
Earth	0.07	500
Mars	0.32	24
Titan	36	2900

Appendix E
Spectral Decomposition of the Transient Eddy Momentum Flux Convergence

We show how the TE term in Equation (30) is decomposed into contributions from eddies of different properties. The transient part of a given field A is Fourier-transformed in longitude and time:

$$A^\dagger(t, \lambda, \phi) = \Re\sum_{k=0}^{N} e^{ik\lambda}\int_{-\infty}^{+\infty} \tilde{A}(\omega, k, \phi)e^{-i\omega t}d\omega, \tag{E1}$$

where N is the maximum resolved zonal wavenumber. We subsequently neglect the contribution from wavenumber 0 (i.e., time variations in the zonal-mean flow), as it is negligible in these simulations. The correlation between two fields $A^\dagger$ and $B^\dagger$ is decomposed as

$$[\overline{A^\dagger B^\dagger}] = \frac{1}{2}\sum_{k=1}^{N}\int_{-\infty}^{+\infty} \Re(\tilde{A}(\omega, k, \phi)\tilde{B}^*(\omega, k, \phi))d\omega. \tag{E2}$$

This way, we decompose the transient EMFC at each latitude as

$$\begin{aligned} \text{TE}(\phi) &= \text{Ro}_T([\overline{\zeta_1^\dagger v_1^\dagger}] - [\overline{\omega^\dagger(u_2 - u_1)^\dagger}]) \\ &= \sum_{k=1}^{N}\int_{-\infty}^{+\infty} K_{k,\omega}(\phi)d\omega, \end{aligned} \tag{E3}$$

where

$$K_{k,\omega}(\phi) = \frac{\text{Ro}_T}{2}\Re(\tilde{\zeta}_1\tilde{v}_1^* + \tilde{\omega}(\tilde{u}_1^* - \tilde{u}_2^*)) \tag{E4}$$

denotes the contribution of waves of frequency ω and zonal wavenumber k to EMFC at latitude ϕ. In Figure 14, we show averages of $K_{k,\omega}(\phi)$ over the equatorial region.

In Section 4.1, we further decompose TE(ϕ) as

$$\mathrm{TE}(\phi) = \int_{-\infty}^{+\infty} \sum_{k=1}^{N} K_{k,c}(\phi) dc, \tag{E5}$$

where $c = \omega \cos\phi/(k\mathrm{Ro}_T)$ is the phase speed (the factor $1/\mathrm{Ro}_T$ comes from our choice of nondimensionalization for velocities) and $K_{k,c} = (k\mathrm{Ro}_T/\cos\phi)K_{k,\omega}$. Figures 6(c) and (f) and Figures 7(c) and (f) show $\sum_{k=1}^{N} K_{k,c}(\phi)$ as a function of c and ϕ.

ORCID iDs

Quentin Nicolas https://orcid.org/0000-0002-4116-973X
Geoffrey K. Vallis https://orcid.org/0000-0002-5971-8995

References

Agol, E., Dorn, C., Grimm, S. L., et al. 2021, Refining the Transit-Timing and Photometric Analysis of TRAPPIST-1: Masses, Radii, Densities, Dynamics, and Ephemerides, PSJ, 2, 1

Baldwin, M. P., Gray, L. J., Dunkerton, T. J., et al. 2001, The Quasi-biennial Oscillation, RvGeo, 39, 179

Barnes, R. 2017, Tidal Locking of Habitable Exoplanets, CeMDA, 129, 509

Barpanda, P., Tulich, S. N., Dias, J., & Kiladis, G. N. 2023, The Role of Subtropical Rossby Waves in Amplifying the Divergent Circulation of the Madden–Julian Oscillation, JAtS, 80, 2377

Bézard, B., Vinatier, S., & Achterberg, R. K. 2018, Seasonal Radiative Modeling of Titan's Stratospheric Temperatures at Low Latitudes, Icar, 302, 437

Bonomo, A. S., Borsato, L., Rajpaul, V. M., et al. 2025, In-Depth Characterization of the Kepler-10 Three-Planet System with HARPS-N Radial Velocities and Kepler Transit Timing Variations, A&A, 696, A233

Bourrier, V., Dumusque, X., Dorn, C., et al. 2018, The 55 Cancri System Reassessed, A&A, 619, A1

Brogi, M., Kok, R. d., Albrecht, S., et al. 2016, Rotation and Winds of Exoplanet HD 189733 b Measured with High-Dispersion Transmission Spectroscopy, ApJ, 817, 106

Burns, K. J., Vasil, G. M., Oishi, J. S., Lecoanet, D., & Brown, B. P. 2020, Dedalus: A Flexible Framework for Numerical Simulations with Spectral Methods, PhRvR, 2, 023068

Cadieux, C., Plotnykov, M., Doyon, R., et al. 2024, New Mass and Radius Constraints on the LHS 1140 Planets: LHS 1140 b Is Either a Temperate Mini-Neptune or a Water World, ApJL, 960, L3

Cohen, M., Bollasina, M. A., Sergeev, D. E., Palmer, P. I., & Mayne, N. J. 2023, Traveling Planetary-Scale Waves Cause Cloud Variability on Tidally Locked Aquaplanets, PSJ, 4, 68

Dias Pinto, J. R., & Mitchell, J. L. 2014, Atmospheric Superrotation in an Idealized GCM: Parameter Dependence of the Eddy Response, Icar, 238, 93

Gill, A. E. 1980, Some Simple Solutions for Heat-Induced Tropical Circulation, QJRMS, 106, 447

Haberle, R. M., Houben, H., Barnes, J. R., & Young, R. E. 1997, A Simplified Three-Dimensional Model for Martian Climate Studies, JGR, 102, 9051

Hammond, M., & Pierrehumbert, R. 2017, Linking the Climate and Thermal Phase Curve of 55 Cancri e, ApJ, 849, 152

Hammond, M., & Pierrehumbert, R. T. 2018, Wave-Mean Flow Interactions in the Atmospheric Circulation of Tidally Locked Planets, ApJ, 869, 65

Hammond, M., Tsai, S.-M., & Pierrehumbert, R. T. 2020, The Equatorial Jet Speed on Tidally Locked Planets. I. Terrestrial Planets, ApJ, 901, 78

Held, I. M., & Suarez, M. J. 1978, A Two-Level Primitive Equation Atmospheric Model Designed for Climatic Sensitivity Experiments, JAtS, 35, 206

Held, I. M., & Suarez, M. J. 1994, A Proposal for the Intercomparison of the Dynamical Cores of Atmospheric General Circulation Models, BAMS, 75, 1825

Hide, R. 1969, Dynamics of the Atmospheres of the Major Planets with an Appendix on the Viscous Boundary Layer at the Rigid Bounding Surface of an Electrically-Conducting Rotating Fluid in the Presence of a Magnetic Field, JAtS, 26, 841

Iga, S., & Matsuda, Y. 2005, Shear Instability in a Shallow Water Model with Implications for the Venus Atmosphere, JAtS, 62, 2514

Innes, H., & Pierrehumbert, R. T. 2022, Atmospheric Dynamics of Temperate Sub-Neptunes. I. Dry Dynamics, ApJ, 927, 38

Kaspi, Y., Galanti, E., Showman, A. P., et al. 2020, Comparison of the Deep Atmospheric Dynamics of Jupiter and Saturn in Light of the Juno and Cassini Gravity Measurements, SSRv, 216, 84

Komacek, T. D., & Showman, A. P. 2019, Temporal Variability in Hot Jupiter Atmospheres, ApJ, 888, 2

Kraucunas, I., & Hartmann, D. L. 2005, Equatorial Superrotation and the Factors Controlling the Zonal-Mean Zonal Winds in the Tropical Upper Troposphere, JAtS, 62, 371

Lewis, N. T., Lombardo, N. A., Read, P. L., & Lora, J. M. 2023, Equatorial Waves and Superrotation in the Stratosphere of a Titan General Circulation Model, PSJ, 4, 149

Liu, B., & Showman, A. P. 2013, Atmospheric Circulation of Hot Jupiters: Insensitivity to Initial Conditions, ApJ, 770, 42

Lutsko, N. J. 2018, The Response of an Idealized Atmosphere to Localized Tropical Heating: Superrotation and the Breakdown of Linear Theory, JAtS, 75, 3

Matsuno, T. 1966, Quasi-geostrophic Motions in the Equatorial Area, JMeSJ, 44, 25

Merlis, T. M., & Schneider, T. 2010, Atmospheric Dynamics of Earth-Like Tidally Locked Aquaplanets, JAMES, 2, 1

Mitchell, J. L., & Lora, J. M. 2016, The Climate of Titan, AREPS, 44, 353

Mitchell, J. L., & Vallis, G. K. 2010, The Transition to Superrotation in Terrestrial Atmospheres, JGRE, 115, E12008

Nicolas, Q. 2026, Code for two-level Dedalus simulations of planetary atmospheres and their analysis, v0.1.1, Zenodo, doi:10.5281/zenodo.19050783

Ohno, K., & Zhang, X. 2019, Atmospheres on Nonsynchronized Eccentric-Tilted Exoplanets. I. Dynamical Regimes, ApJ, 874, 1

Peixoto, J. P., & Oort, A. H. 1992, Physics of Climate (1st ed.; AIP)

Perez-Becker, D., & Showman, A. P. 2013, Atmospheric Heat Redistribution on Hot Jupiters, ApJ, 776, 134

Pierrehumbert, R. T., & Hammond, M. 2019, Atmospheric Circulation of Tide-Locked Exoplanets, AnRFM, 51, 275

Potter, S. F., Vallis, G. K., & Mitchell, J. L. 2014, Spontaneous Superrotation and the Role of Kelvin Waves in an Idealized Dry GCM, JAtS, 71, 596

Randel, W. J., & Held, I. M. 1991, Phase Speed Spectra of Transient Eddy Fluxes and Critical Layer Absorption, JAtS, 48, 688

Saravanan, R. 1993, Equatorial Superrotation and Maintenance of the General Circulation in Two-Level Models, JAtS, 50, 1211

Seager, R., Harnik, N., Kushnir, Y., Robinson, W., & Miller, J. 2003, Mechanisms of Hemispherically Symmetric Climate Variability, JCli, 16, 2960

Showman, A. P., Cooper, C. S., Fortney, J. J., & Marley, M. S. 2008, Atmospheric Circulation of Hot Jupiters: Three-Dimensional Circulation Models of HD 209458b and HD 189733b with Simplified Forcing, ApJ, 682, 559

Showman, A. P., Fortney, J. J., Lian, Y., et al. 2009, Atmospheric Circulation of Hot Jupiters: Coupled Radiative-Dynamical General Circulation Model Simulations of HD 189733b and HD 209458b, ApJ, 699, 564

Showman, A. P., & Polvani, L. M. 2010, The Matsuno-Gill Model and Equatorial Superrotation, GeoRL, 37, L18811

Showman, A. P., & Polvani, L. M. 2011, Equatorial Superrotation on Tidally Locked Exoplanets, ApJ, 738, 71

Stassun, K. G., Collins, K. A., & Gaudi, B. S. 2017, Accurate Empirical Radii and Masses of Planets and Their Host Stars with Gaia Parallaxes, AJ, 153, 136

Suarez, M. J., & Duffy, D. G. 1992, Terrestrial Superrotation: A Bifurcation of the General Circulation, JAtS, 49, 1541

Takagi, M., & Matsuda, Y. 2007, Effects of Thermal Tides on the Venus Atmospheric Superrotation, JGRD, 112, D09112

Torrence, C., & Compo, G. P. 1998, A Practical Guide to Wavelet Analysis, BAMS, 79, 61

Tsai, S.-M., Dobbs-Dixon, I., & Gu, P.-G. 2014, Three-Dimensional Structures of Equatorial Waves and the Resulting Super-rotation in the Atmosphere of a Tidally Locked Hot Jupiter, ApJ, 793, 141

Vallis, G. K. 2017, Atmospheric and Oceanic Fluid Dynamics: Fundamentals and Large-Scale Circulation (2nd ed.; Cambridge Univ. Press)

Wang, P., & Mitchell, J. L. 2014, Planetary Ageostrophic Instability Leads to Superrotation, GeoRL, 41, 4118

Williams, G. P. 2006, Equatorial Superrotation and Barotropic Instability: Static Stability Variants, JAtS, 63, 1548

Xue, Q., Bean, J. L., Zhang, M., et al. 2024, JWST Thermal Emission of the Terrestrial Exoplanet GJ 1132b, ApJL, 973, L8

Yang, J., & Abbot, D. S. 2014, A Low-Order Model of Water Vapor, Clouds, and Thermal Emission for Tidally Locked Terrestrial Planets, ApJ, 784, 155

Yang, J., Cowan, N. B., & Abbot, D. S. 2013, Stabilizing Cloud Feedback Dramatically Expands the Habitable Zone of Tidally Locked Planets, ApJL, 771, L45

Zurita-Gotor, P., Álvaro Anaya-Benlliure, & Held, I. M. 2022, The Sensitivity of Superrotation to the Latitude of Baroclinic Forcing in a Terrestrial Dry Dynamical Core, JAtS, 79, 1311

Zurita-Gotor, P., & Held, I. M. 2018, The Finite-Amplitude Evolution of Mixed Kelvin–Rossby Wave Instability and Equatorial Superrotation in a Shallow-Water Model and an Idealized GCM, JAtS, 75, 2299